The Astrophysical Journal, 744:34 (22pp), 2012 January 1 doi:10.1088/0004-637X/744/1/34

MODELING PHASE-ALIGNED GAMMA-RAY AND RADIO MILLISECOND PULSAR LIGHT CURVES

C. Venter[1], T. J. Johnson[2,3,4], and A. K. Harding[2]
[1] Centre for Space Research, North-West University, Potchefstroom Campus, Potchefstroom 2520, South Africa
[2] Astrophysics Science Division, NASA Goddard Space Flight Center, Greenbelt, MD 20771, USA
[3] Department of Physics, University of Maryland, College Park, MD 20742, USA
Received 2011 March 24; accepted 2011 October 17; published 2011 December 12

ABSTRACT

Since the discovery of the first eight gamma-ray millisecond pulsars (MSPs) by the *Fermi* Large Area Telescope, this population has been steadily expanding. Four of the more recent detections, PSR J0034−0534, PSR J1939+2134 (B1937+21; the first MSP ever discovered), PSR J1959+2048 (B1957+20; the first discovery of a black widow system), and PSR J2214+3000, exhibit a phenomenon not present in the original discoveries: nearly phase-aligned radio and gamma-ray light curves (LCs). To account for the phase alignment, we explore models where both the radio and gamma-ray emission originate either in the outer magnetosphere near the light cylinder or near the polar caps. Using a Markov Chain Monte Carlo technique to search for best-fit model parameters, we obtain reasonable LC fits for the first three of these MSPs in the context of "altitude-limited" outer gap (alOG) and two-pole caustic (alTPC) geometries (for both gamma-ray and radio emission). These models differ from the standard outer gap (OG)/two-pole caustic (TPC) models in two respects: the radio emission originates in caustics at relatively high altitudes compared to the usual conal radio beams, and we allow both the minimum and maximum altitudes of the gamma-ray and radio emission regions to vary within a limited range (excluding the minimum gamma-ray altitude of the alTPC model, which is kept constant at the stellar radius, and that of the alOG model, which is set to the position-dependent null charge surface altitude). Alternatively, phase-aligned solutions also exist for emission originating near the stellar surface in a slot gap scenario ("low-altitude slot gap" (laSG) models). We find that the alTPC models provide slightly better LC fits than the alOG models, and both of these give better fits than the laSG models (for the limited range of parameters considered in the case of the laSG models). Thus, our fits imply that the phase-aligned LCs are likely of caustic origin, produced in the outer magnetosphere, and that the radio emission for these pulsars may come from close to the light cylinder. In addition, we were able to constrain the minimum and maximum emission altitudes with typical uncertainties of ∼30% of the light cylinder radius. Our results therefore describe a third gamma-ray MSP subclass, in addition to the two previously found by Venter et al.: those with LCs fit by standard OG/TPC models and those with LCs fit by pair-starved polar cap models.

Key words: acceleration of particles – gamma rays: stars – pulsars: individual (PSR J0034−0534, PSR J1939+2134, PSR J1959+2-48) – radiation mechanisms: non-thermal

Online-only material: color figures

1. INTRODUCTION

The *Fermi* Large Area Telescope (LAT) has recently released a catalog of 46 gamma-ray pulsars (Abdo et al. 2010a) including eight millisecond pulsars (MSPs; Abdo et al. 2009). The number of gamma-ray pulsars is steadily growing, with the total number of gamma-ray MSPs now at least 20 (Guillemot et al. 2011) and the full population of gamma-ray pulsars exceeding 70 (Romani 2011). Detection of PSR J0034−0534 (Abdo et al. 2010b) revealed it to be the first MSP to have (nearly) phase-aligned radio and gamma-ray light curves (LCs). Previously, this has only been observed for the Crab pulsar (Kniffen et al. 1974). Subsequent discovery of gamma-ray pulsations from PSR J1939+2134 (B1937+21), PSR J1959+2048 (B1957+20; Guillemot et al. 2012), and PSR J2214+3000 (Ransom et al. 2011) confirmed this rare behavior for three more MSPs.

Traditionally, two types of models have been invoked to explain high-energy (HE) radiation from (mostly younger) pulsars. Polar cap (PC) models (e.g., Daugherty & Harding 1982, 1996) assume injection of primary electrons from the neutron star (NS) surface and subsequent magnetic pair production of the resulting curvature radiation or inverse-Compton-scattered gamma rays (upscattered thermal X-rays) in the intense B-fields close to the NS surface (at radius $R_{\rm NS}$). A slot gap (SG; Arons 1983; Muslimov & Harding 2003, 2004a) may also form along the last open B-field lines of the pulsar magnetosphere in the absence of pair creation along those lines. This corresponds to a two-pole caustic (TPC) geometry (Dyks & Rudak 2003) which may extend from the NS surface up to near the light cylinder $R_{\rm LC}$. Second, outer gap (OG) models (e.g., Cheng et al. 1986a, 1986b; Romani 1996) assume that HE radiation is produced along the last open field lines above the null charge surface (NCS) where the Goldreich–Julian charge density changes sign (although see Hirotani 2006, 2007 for an OG solution which extends toward the NS surface, beyond the NCS). The HE pulse profiles in outer-magnetosphere models are the result of the formation of caustics, i.e., the accumulation of photons in narrow phase bands due to a combination of special relativistic effects and B-line curvature. The narrow gaps in the OG and TPC models require screening of the electric field parallel to the local B-field by high pair multiplicity, and therefore presuppose copious pair production. Lastly, Bai & Spitkovsky (2010) also modeled HE LCs in the context of OG and TPC models in a force-free B-field geometry, proposing a separatrix layer model close to $R_{\rm LC}$.

[4] National Research Council Research Associate, National Academy of Sciences, Washington, DC 20001, USA; resident at Naval Research Laboratory, Washington, DC 20375, USA.

In the case of MSPs, LCs and spectra have been modeled (e.g., Frackowiak & Rudak 2005; Harding et al. 2005; Venter & De Jager 2005) using a pair-starved polar cap (PSPC) model (Muslimov & Harding 2004b, 2009), an extension of the traditional PC model, where the magnetic pair multiplicity is not high enough to screen the accelerating electric field and the open volume above the PC is therefore pair-starved. Primary electrons are accelerated up to very high altitudes above the full PC, while pair formation is suppressed. MSP spectra and energetics have also been modeled in the context of an OG model (Zhang & Cheng 2003; Zhang et al. 2007). The annular gap model of Du et al. (2010) can furthermore reproduce the main characteristics of the gamma-ray LCs of three MSPs, although this model does not attempt to model the non-zero phase offsets between the gamma-ray and radio profiles.

Venter et al. (2009) recently modeled the first eight *Fermi*-detected gamma-ray MSPs and found the emergence of two distinct MSP subclasses: those whose LCs are well fit by a standard OG or a TPC model and those whose LCs are well fit by a PSPC model (with these fits being mutually exclusive). Importantly, the OG/TPC and PSPC models yielded the correct radio-to-gamma phase lags for these eight MSPs when the radio emission was modeled as a cone beam at lower altitude. A significant and unexpected conclusion from this study was that MSPs have screened magnetospheres with large amounts of pairs available, as these conditions are needed to set up the gap structure presupposed by the OG/TPC models. This is in contrast to the previous notion that most MSPs have pair-starved magnetospheres (Harding et al. 2005; Venter & De Jager 2005), which follows from pair death line calculations using the standard (relatively low) dipole B-field values inferred for MSPs. Harding & Muslimov (2011) have demonstrated that small distortions of the dipole B-field cause offsets of the PC enhance pair creation, even in MSPs, and may therefore provide a mechanism for creating such gaps even in low spin-down pulsars.

The near phase alignment of the gamma-ray and radio LCs of PSR J0034−0534, PSR J1939+2134, and PSR J1959+2048, however, argues for overlapping emission regions of the radio and gamma rays, thereby departing from the behavior of the two MSP subclasses found by Venter et al. (2009; Section 3). These new phase-aligned LCs therefore motivate the investigation of co-located radio and gamma-ray emission regions, either near to $R_{\rm NS}$ or closer to $R_{\rm LC}$ (Manchester 2005).

Additional motivation for studying caustic radio emission close to $R_{\rm LC}$ comes from the study of Ravi et al. (2010). Following the large number of gamma-ray pulsar detections by *Fermi* LAT, they investigated beaming properties of gamma-ray-selected as well as radio-selected normal pulsars and MSPs, i.e., those detected (or detectable) using blind searches for periodicity on *Fermi* data and those detectable in blind radio searches. By studying the relative number of gamma-ray to radio pulsars for each of these two samples, they conclude that radio and gamma-ray beams must have comparable sky coverage (close to 4π sr) for pulsars with high spin-down luminosities ($\dot{E}_{\rm rot} \gtrsim 10^{37}$ erg s^{-1}), while radio beams shrink to roughly half the typical gamma-ray beam sizes for lower-$\dot{E}_{\rm rot}$ pulsars (with $\dot{E}_{\rm rot} \lesssim 5 \times 10^{35}$ erg s^{-1}) and eventually decrease to ∼10% of the gamma-ray beam size for older pulsars. An important implication is that the radio emission should originate in wide beams at a significant fraction of $R_{\rm LC}$. Ravi et al. (2010) therefore comment that modeling of radio pulse profiles as caustics using outer-magnetospheric (specifically SG) geometries for both young pulsars and MSPs will be valuable for testing the plausibility of their conclusions. (Interestingly, Dyks et al. 2010 have studied the influence of rotation on MSP profiles, presenting analytical results for a static dipole B-field geometry that are applicable for low altitudes or small angles from the dipole axis and may be applied to both caustic radio and caustic gamma-ray emission. They demonstrate the existence of a caustic phase on the trailing side where maximum bunching of radiation occurs, beyond which no emission can be observed and which coincides with the steepest gradient of the polarization angle, while the curvature radiation emissivity may be a minimum at this phase.) However, LCs resulting from radio and gamma-ray caustics would generally be nearly phase-aligned (although small phase differences of ∼0.2 could result from the radio and gamma-ray emission regions being at different altitudes). Among the young *Fermi* pulsars, only the fastest Crab pulsar shows phase-aligned radio and gamma-ray pulses, while the others show quite large (∼0.1–0.5) radio-to-gamma-ray phase lags. It therefore seems that, while the idea of wide radio beams may be valid, caustic emission probably is not as widespread in young pulsars that have large LC lags. (Pulsar population modeling will be able to better quantify this statement as well as multi-wavelength polarization studies; see Section 6). On the other hand, in the case of the MSPs with even smaller periods, radio caustics may be more common, as there are many more examples of pulsars with phase-aligned LCs in this group.

In this paper, we investigate the possibility of reproducing phase-aligned radio and gamma-ray LCs using "altitude-limited" OG/TPC models (alOG/alTPC) in which we limit the extent of the emission regions (Section 3.1) versus a low-altitude SG (laSG) model (Section 3.2). We apply our results to PSR J0034−0534, PSR J1939+2134, and PSR J1959+2048 and infer values for the magnetic inclination and observer angles α and ζ from the best-fit LCs in each case (Section 5) using a Markov Chain Monte Carlo (MCMC) technique (Section 4). Our conclusions follow in Section 6.

2. BACKGROUND ON MSPs WITH ALIGNED RADIO AND GAMMA-RAY EMISSION

2.1. PSR J0034−0534

Bailes et al. (1994) announced the discovery of the 1.87 ms MSP PSR J0034−0534 with the Parkes telescope together with two other southern sky MSPs, all of which are in binary systems following circular orbits with low-mass companions. PSR J0034−0534's rotational age ($\tau_{\rm c} = P/2\dot{P} \sim 10$ Gyr), dipolar surface field ($B_0 \sim 10^8$ G), and spin-down power $\dot{E}_{\rm rot} \sim 2 \times 10^{34}$ erg s^{-1} (Abdo et al. 2010b) are typical among the radio MSP population. It is also relatively close, lying at 0.5 kpc (Hobbs et al. 2005). A power-law spectrum with an index of 2.6 for the frequency range 102 MHz to 4.8 GHz was obtained by Kuzmin & Losovsky (2001). Its large B-field at the light cylinder $B_{\rm LC}$ prompted giant pulse emission searches, but no giant pulses have been found (e.g., Knight et al. 2005). Furthermore, no rotating vector model (RVM) fits exist for PSR J0034−0534 (Stairs et al. 1999) and no infrared to far-infrared emission from putative dust disks around PSR J0034−0534 have been observed (Greaves & Holland 2000; Lazio & Fischer 2004). *Hubble Space Telescope* observations revealed an optical white dwarf companion with a mass of about $0.2\,M_{\odot}$, an effective temperature 3250 K $\leqslant T_{\rm eff} <$ 3800 K, and a cooling time which is consistent with $\tau_{\rm c}$ (Bell et al.

1995; Lundgren et al. 1996). This is similar to the results of Hansen & Phinney (1998) who estimated a companion mass of 0.15–0.32 $M_\odot$ and $T_{\rm eff} < 3500$ K assuming a He core, while Schönberner et al. (2000) argued for a $\approx$0.5 $M_\odot$ companion with a CO core based on evolutionary model calculations. Zavlin (2006) reported a $<3\sigma$ detection of an X-ray source 0.″2 from the pulsar position by *XMM-Newton*, although no spectral or temporal information could be extracted due to the presence of a very bright object in the same field of view. The *EGRET* 3σ flux upper limit above 100 MeV (Fierro et al. 1995) exceeds the recent *Fermi* measurements (Abdo et al. 2010b) of 2.7×10^{-8} cm^{-2} s^{-1} by an order of magnitude.

2.2. PSR J1939+2134 (B1937+21)

PSR J1939+2134 is the first MSP ever discovered (Backer et al. 1982), which interestingly, lies close to the first pulsar ever discovered, PSR B1919+21 (Hewish et al. 1968). With its period $P = 1.558$ ms, it remains one of the fastest-spinning MSPs discovered to date. Using its period-derivative $\dot{P} \approx 1.05 \times 10^{-19}$ s s^{-1}, one obtains a very high spin-down luminosity of $\dot{E}_{\rm rot} \approx 10^{36}$ erg s^{-1}, surface B-field of $B_0 \sim 4 \times 10^8$ G, and a characteristic age of $\tau_{\rm c} \sim 0.2$ Gyr (Manchester et al. 2005). Verbiest et al. (2009) measured a proper motion of $\approx$0.4 mas yr^{-1} and a timing parallax of 0.13 ± 0.07 implying a distance of $d = 7.7 \pm 3.8$ kpc (Guillemot et al. 2012). *RXTE* observations (Cusumano 2003) revealed a double-peaked X-ray profile with a phase separation of about half a rotation (see also Nicastro et al. 2004), closely aligned with the phases of the microsecond-duration, power-law-distributed giant pulses (e.g., Kinkhabwala & Thorsett 2000), but slightly lagging the radio peaks. Cusumano (2003) furthermore fit the pulsed spectrum in the 2–25 keV range using a power law with index $\sim$1.1. PSR J1939+2134, along with PSR J0218+4232, PSR B1821−24, and PSR J1959+2048 belong to a group termed "Class II" by Kuiper et al. (2000) and Kuiper & Hermsen (2003). MSPs in Class II have high X-ray luminosities, hard spectra, and narrow pulses, while those in "Class I" have low X-ray luminosities, soft, thermal-dominated spectra, and broad pulses (e.g., PSR J0030+0451, PSR J0437−4715, PSR J1024−0719, and PSR J2124−3358). Zavlin (2006, 2007) elaborated on these two distinct groups of X-ray-emitting MSPs. The non-thermally emitting X-ray MSPs have high spin-down luminosities ($\dot{E}_{\rm rot} > 10^{35}$ erg s^{-1}), short periods ($P \lesssim 3$ ms), power-law spectra in the keV band (usually interpreted as synchrotron or inverse Compton radiation), and strong, narrow X-ray pulse profiles with large pulsed fractions nearly in phase with the radio. On the other hand, the thermally emitting MSPs are less energetic with spin-down powers $\dot{E}_{\rm rot} \lesssim 10^{34}$ erg s^{-1}, their X-ray spectra are not well fit by power laws alone but have a predominantly thermal PC component, and they exhibit lower pulsed fractions. Fierro et al. (1995) gave a 3σ upper limit to the unpulsed flux above 100 MeV of 15.1×10^{-8} cm s^{-1}, while pulsations with a significance well above 5σ have now been detected from PSR J1939+2134 by *Fermi* (Guillemot et al. 2012).

2.3. PSR J1959+2048 (B1957+20)

PSR J1959+2048 with $P = 1.607$ ms is the first "black widow" pulsar discovered in a nearly circular eclipsing binary orbit in which the tidally locked companion star (Fruchter et al. 1988a; Van Paradijs 1988) with a very small mass of $\sim$0.025 $M_\odot$ is being oblated by the compact object (Fruchter et al. 1988b; Phinney et al. 1988; Callanan et al. 1995), giving credence to the recycling scenario for the formation of MSPs (Alpar et al. 1982). Its distance is estimated to be $d \sim 2.5$ kpc, and its intrinsic $\dot{P}$ is $\sim 8 \times 10^{-21}$ (Guillemot et al. 2012), leading to a spin-down luminosity of $\dot{E}_{\rm rot} \sim 7 \times 10^{34}$ erg s^{-1}, surface B-field of $B_0 \sim 10^8$ G, and a characteristic age of $\tau_{\rm c} \sim 3$ Gyr. Kulkarni & Hester (1988) discovered an Hα emission nebula surrounding PSR J1959+2048, implying interaction of the relativistic pulsar wind and the interstellar medium. Subsequently, an X-ray tail of at least 16″ corresponding to the shocked pulsar wind has been seen extending from the pulsar, interior to the Hα nebula (Stappers et al. 2003). Using *XMM-Newton*, Huang & Becker (2007) fit a power-law spectrum of index $\sim$2.0 and found a phase dependence of the X-ray emission on the binary orbital period (as was the case for earlier optical and infrared observations; Van Paradijs 1988; Eales et al. 1990), although they could not detect any pulsations at the pulsar spin period. However, $\sim 4\sigma$ X-ray pulsations have now been observed from PSR J1959+2048, with the X-ray peaks seemingly in close alignment with the radio peaks (Guillemot et al. 2012). No significant gamma-ray emission has been observed (Acharya et al. 1990; Brink et al. 1990; Fierro et al. 1995; Buccheri et al. 1996; Hall et al. 2003) prior to *Fermi* (Guillemot et al. 2012).

2.4. Other MSPs That May Have Phase-aligned Profiles

See Table 1 for a list of parameters of all the MSPs from which gamma-ray pulsations have been observed by *Fermi* and which have been announced publicly. MSPs such as PSR B1821−24 and PSR J0737−3039A plausibly have phase-aligned radio and gamma-ray LCs on the basis that their radio and X-ray profiles are phase-aligned (Backer & Sallmen 1997; Chatterjee et al. 2007). Profile phase alignment would imply that emission across all these different wavebands originates in similar regions in the pulsar magnetosphere. While two peaks in the X-ray profile are aligned with two of the three pulses visible at radio frequencies for PSR J0218+4232 (Kuiper et al. 2004), there is a non-zero lag between its radio and gamma-ray profiles (Abdo et al. 2009).

3. DESCRIPTION OF GEOMETRIC MODELS

Venter et al. (2009) found that the LCs of six gamma-ray MSPs could be modeled using standard OG and TPC models (and invoking a single-altitude radio conal beam geometry centered on the magnetic axis), and found fits for α and ζ, measured with respect to the spin axis. The gamma-ray LCs of these MSPs are preceded by a radio pulse leading by $\sim$0.2–0.5 in normalized rotational phase. These phase offsets argue for the case where radio emission comes from a different (lower) emission region, while the gamma-ray emission originates over an extended range of altitudes, including altitudes close to $R_{\rm LC}$. An extended emission region is required to create the intense caustics (Morini 1983) which give rise to the peaks in the LCs for outer-magnetospheric pulsar models. On the other hand, the LCs of two other MSPs were fit by PSPC-predicted profiles, where the radio lags the gamma-ray profiles by $\sim$0.2 in phase. This again required radio emission from lower altitudes, and gamma-ray emission from a range of altitudes, over the full open volume above the PC.

MSPs with phase-aligned LCs, however, disqualify the above scenarios for their emission: phase alignment implies co-location of emission regions across wavebands (Abdo et al. 2010b). The question is whether both the gamma rays and radio occur in extended high-altitude regions (Section 3.1), or at low altitudes (Section 3.2). In what follows, we describe models for

Table 1
Parameters of Several Gamma-Ray MSPs

Name	P (ms)	$\dot{P}$ (10^{-20})	Distance (kpc)	Age[a] (10^9 yr)	$\dot{E}_{\rm rot}$[b] (10^{33} erg s^{-1})	B_0[c] (10^8 G)	BS[d]	LC Class[e]	References
J0030+0451	4.865	1.01	0.300 ± 0.090	7.63	3.47	2.24	No	I	1
J0034−0534	1.877	0.259	$0.54\ ^{+0.22}_{-0.14}$	11.5	15.5	0.706	Yes	II	2
J0218+4232	2.323	7.79	2.70 ± 0.60	0.47	245	4.31	Yes	I	1
J0437−4715	5.757	1.39	0.156 ± 0.002	6.55	2.88	2.87	Yes	I	1
J0613−0200	3.061	0.915	0.48 ± 0.14	5.31	12.6	1.69	Yes	I	1
J0614−3329	3.148	1.75	1.9	2.8	22.2	2.4	Yes	I[f]	3
J0751+1807	3.479	0.755	0.62 ± 0.31	7.30	7.08	1.64	Yes	I	1
J1231−1411	3.684	2.28	0.4	2.6	18.0	2.9	Yes	I[f]	3
J1614−2230	3.151	0.397	1.30 ± 0.25	12.6	5.01	1.13	Yes	I	1
J1744−1134	4.075	0.682	0.470 ± 0.090	9.47	3.98	1.69	Yes	III	1
J1939+2134	1.558	10.5	7.7 ± 3.8	0.235	1098	4.09	Yes	II	4
J1959+2048	1.607	1.685	2.5 ± 1.0	1.51	74.7	1.12	Yes	II	4
J2017+0603	2.896	0.83	1.56	5.55	13.43	1.57	Yes	I	5
J2124−3358	4.931	1.21	0.25 ± 0.13	6.47	3.98	2.47	Yes	III	1
J2214+3000	3.119	1.40	1.5	3.5	17.3	2.1	Yes	II[f]	3
J2302+4442	5.192	1.33	1.18	6.20	3.74	2.66	Yes	I	5

Notes.
[a] Characteristic rotational age, using $\tau = P/2\dot{P}$.
[b] Rotational spin-down power.
[c] Surface B-field, using $B_0 \approx 3.2 \times 10^{19}\sqrt{P\dot{P}}$ G.
[d] In a binary system?
[e] MSP gamma-ray LC class (not to be confused with the two classes of X-ray MSPs defined by Kuiper et al. 2000): Class I (standard OG/TPC models; gamma-ray profile lags radio), Class II (alOG/alTPC models; phase-aligned LCs), and Class III (PSPC models; gamma-ray profile precedes radio).
[f] From PhD thesis of T. J. Johnson.
References. (1) Abdo et al. 2009; (2) Abdo et al. 2010b; (3) Ransom et al. 2011; (4) Guillemot et al. 2012; (5) Cognard et al. 2011.

both cases (we first alluded to these models in Abdo et al. 2010b) and report our model LC results in Section 5.

As in the past, we use the retarded vacuum dipole field as the basic structure of the pulsar magnetosphere (e.g., Deutsch 1955; Dyks et al. 2004). Although the field structure of young pulsars may be closer to force free (Spitkovsky 2006), it is not clear whether MSPs produce the pair multiplicity required for force-free magnetospheres. We also assume that the photon emission rate is constant along field lines in the corotating frame, and therefore do not explicitly include an E-field or particle transport calculations, as we are primarily concerned with reproducing LCs and thereby constraining emission locations of the radio and gamma-ray radiation in the pulsar magnetosphere. Our geometric models treat relativistic effects such as aberration of photon directions and B-field structure consistently to first order in $r/R_{\rm LC}$ (with r the radial distance from the NS center, and $R_{\rm LC} = c/\Omega = cP/2\pi$ the light cylinder), but we include the Lorentz transformation of the local B-field between lab and corotating frames (Bai & Spitkovsky 2010). However, our OG and TPC models are not changed significantly by this transformation, as it is a second-order effect in $r/R_{\rm LC}$.

Short-period MSP magnetospheres are quite small, with light cylinder radii on the order of 10 stellar radii:

$$\frac{R_{\rm LC}}{R_{\rm NS}} = \frac{9.55 P_{2\rm ms}}{R_6}, \quad (1)$$

with $R_6 = R_{\rm NS}/10^6$ cm the stellar radius and $P_{2\,\rm ms} = P/0.002$ s. It is therefore plausible that the radio emission may originate at a larger altitude relative to $R_{\rm LC}$ in MSPs (Manchester 2005), as opposed to the case of young pulsars, where the radio emission is believed to originate at smaller altitudes relative to $R_{\rm LC}$. (Ravi et al. 2010, however, make the argument that radio beams of gamma-ray pulsars might occur high up in the magnetosphere, but this may lead to radio and gamma-ray LCs with small phase lags. See Sections 1 and 6.)

3.1. High-altitude Gamma-Ray and Radio Emission: Altitude-limited OG (alOG) and TPC (alTPC) Models

For this class of models, we are using the same framework as Venter et al. (2009), except that the radio emission region is extended in altitude, and we limit the minimum and maximum radii of the radio and gamma-ray emission regions. (We previously used $(R^{\gamma}_{\rm min}, R^{\gamma}_{\rm max}) = (R_{\rm NS}, 1.2R_{\rm LC})$ for the TPC models and $(R^{\gamma}_{\rm min}, R^{\gamma}_{\rm max}) = (R_{\rm NCS}, 1.2R_{\rm LC})$ for the OG models.) Technically, the traditional OG model is a specific instance of an alOG model, and this is also the case for traditional TPC and alTPC models. For the standard OG model, one typically assumes that the minimum radius for the gamma-ray emission is $R^{\gamma}_{\rm min} = R_{\rm NCS}$, while $R^{\gamma}_{\rm max} \gtrsim R_{\rm LC}$. For the standard TPC model, $R^{\gamma}_{\rm min} = R_{\rm NS}$, while $R^{\gamma}_{\rm max} \gtrsim R_{\rm LC}$. The emission of both of these standard models is restricted to lie within a cylindrical radius $\rho_{\rm max} \lesssim 1.0R_{\rm LC}$. Because of the great similarity, one may in some cases use the terms alOG and OG (or alTPC and TPC) interchangeably when statements apply to both classes of models, or when the meaning is clear from the context.

In contrast to Venter et al. (2009), we do not use an axis-centered radio conal model, but we investigate radio photons coming from an OG/TPC-like structure, i.e., we apply the alOG/alTPC models to both gamma rays and radio. The maximum radius[5] $R_{\rm max}$ represents an upper limit, since in some cases where $R_{\rm max} \sim 1.1R_{\rm LC}$, the emission may not actually go

[5] When necessary, we will distinguish minimum and maximum radii for the gamma-ray versus radio emission using superscripts γ and r, otherwise the particular variable is used generically and refers to both wavelengths. The same holds for $r_{\rm OVC,min}$, $r_{\rm OVC,max}$, as well as emission layer width w, to be defined below.

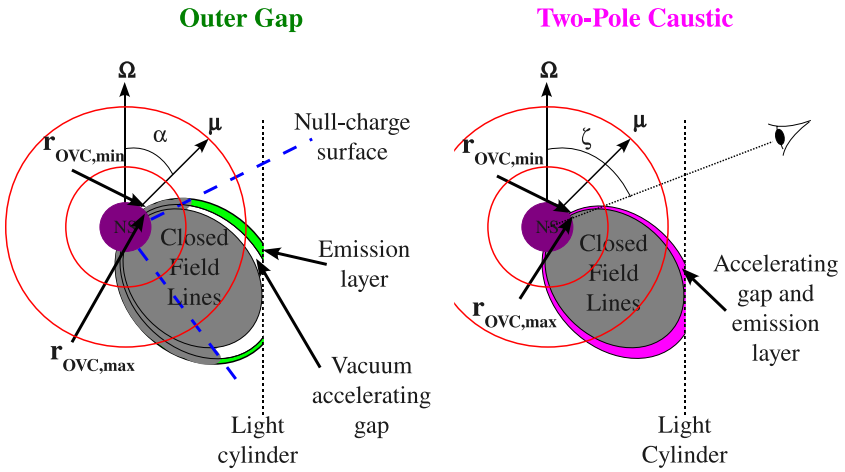

Figure 1. Schematic diagram of the emission layers in the OG (a) and TPC (b) geometries. The magnetic axis is indicated by $\vec{\mu}$ and the spin axis by $\vec{\Omega}$. The two concentric circles indicate the limiting minimum and maximum emission radii imposed for the altitude-limited models (see Section 3.1).
(A color version of this figure is available in the online journal.)

all the way out to $R_{\rm max}$. This is because we limit the extent of the emission according to a cylindrical radius $\rho_{\rm max} < 0.95 R_{\rm LC}$.

For the lower limit, we always ensure that $R_{\rm min} < R_{\rm max}$. This condition is usually met, but it becomes important to enforce at extremely high values of $R_{\rm min}$, as may occur in some cases of radio LC fits. In the alOG radio models, the minimum radius is actually max $\{R_{\rm min}, R_{\rm NCS}\}$, so it is a function of magnetic azimuth ϕ and co-latitude θ when $R_{\rm NCS} > R_{\rm min}$. Here, $R_{\rm NCS}(\theta, \phi)$ is the radius of the NCS. We always set $R^{\gamma}_{\rm min} = R_{\rm NS}$ for alTPC (and TPC) and $R^{\gamma}_{\rm min} = R_{\rm NCS}$ for alOG (and alOG) fits, while $R^{r}_{\rm min}$ may vary and may even be quite close to $R_{\rm LC}$.

Apart from P which determines the size of the PC, our alOG LC fits have nine free parameters ($R^{\gamma}_{\rm min}$ is kept fixed as described earlier, stemming from the prescriptions of the theoretical models): $(\alpha, \zeta, r^{\gamma}_{\rm OVC,min}, r^{\gamma}_{\rm OVC,max}, r^{r}_{\rm OVC,min}, r^{r}_{\rm OVC,max}, R^{\gamma}_{\rm max}, R^{r}_{\rm min}, R^{r}_{\rm max})$. The parameters $r_{\rm OVC,min}$ and $r_{\rm OVC,max}$ are the inner and outer radii in open volume coordinates (OVCs) which demarcate the outer-magnetospheric emission layer boundaries (see Figure 1) formed by retarded dipole B-field lines corresponding to these values (Dyks et al. 2004). The emission layer width is defined as $w \equiv r_{\rm OVC,max} - r_{\rm OVC,min}$. The OVC is approximately the same as the parameter $\xi \equiv \theta/\Theta_{\rm PC}$ (used for the general relativistic dipole field), the polar angle normalized to the PC angle (e.g., Muslimov & Tsygan 1992), which also ranges from 0 to 1 from the magnetic axis up until the last open B-field line. Thus, w approximately gives the transverse width (in the θ-direction) normalized to the PC angle $\Theta_{\rm PC} \sim \sqrt{R/R_{\rm Lc}}$ (this would have been exact if the ξ and $r_{\rm OVC}$ coordinates coincided). The total transverse OG gap width is $1.00 - r_{\rm OVC,min}$, although the emission only comes from a thin layer embedded inside that gap, tangent to its inner boundary, and lying between $r_{\rm OVC,min}$ and $r_{\rm OVC,max}$ as motivated by theoretical considerations (e.g., Wang et al. 2010). This is shown in Figure 1. For the alOG model, we constrain $r_{\rm OVC,min}$ as follows: we require that w not be more than half of the vacuum region $(1.00 - r_{\rm OVC,max})$ of the total gap $(1.00 - r_{\rm OVC,min})$, which leads to $r_{\rm OVC,max} - 0.5(1.00 - r_{\rm OVC,max}) \leqslant r_{\rm OVC,min} \leqslant r_{\rm OVC,max}$. Using a resolution of 0.05 in $r_{\rm OVC}$, this condition results in permissible combinations $(r_{\rm OVC,min}, r_{\rm OVC,max}) = (0.85, 0.90)$, (0.90, 0.90), (0.95, 0.95), and (1.00, 1.00). We sometimes find best-fit values of $w = 0$, which is unphysical, but in reality this means that $w < 0.05$. In contrast, for the alTPC we fix $r_{\rm OVC,max} = 1.00$, as the radiating layer fills the gap and terminates on the last open field line in the standard SG scenario. Furthermore, as the emission layer coincides with the total gap for this case, their respective widths are the same. The alTPC therefore has eight free parameters and we investigate the combinations $(r_{\rm OVC,min}, r_{\rm OVC,max}) = (0.90, 1.00)$, (0.95, 1.00), and (1.00, 1.00). We emphasize that the radio and gamma-ray emission layers are fit independently. This is because the gamma-ray and radio emission might physically originate from distinct particle populations in the magnetosphere; rather than prescribe a particular gap width or position, we try to obtain constraints for these variables from the data, within a particular region of phase space as explained above.

3.2. Low-altitude Gamma-Ray and Radio Emission: Low-altitude Slot Gap (laSG) Models

While the alOG and alTPC models gave good fits to the radio and gamma-ray LCs (Section 5), we decided to also study the possibility of a low-altitude, non-caustic origin of the emission. This scenario may be described by geometric low-altitude slot gap (laSG) models, which are actually very low altitude geometric TPC models resembling a hollow cone beam close to the stellar surface (see, e.g., Muslimov & Harding 2003 for a description of an laSG radiation model). We investigate two different cases, one in which we assume a constant emissivity for the emission and one where the emissivity is modulated according to

$$I \propto \begin{cases} \exp\left(\Delta s/\sigma_{\rm in}\right), & s \leqslant s_{\rm f} \\ \exp\left(-\Delta s/\sigma_{\rm out}\right), & s > s_{\rm f}, \end{cases} \quad (2)$$

with s the distance above the NS surface along a B-field line, $\Delta s \equiv s - s_{\rm f}$, and $\sigma_{\rm in}$ and $\sigma_{\rm out}$ setting the rate at which the intensity rises and falls along the B-field lines. The peak intensity occurs at a distance $s = s_{\rm f}$ (i.e., $\Delta s = 0$) along the field lines. The emissivity profiles of Equation (2) are motivated by detailed modeling of pair creation and He emission using full radiation models (see, e.g., Muslimov & Harding 2003). For example, this results in typical values for $s_{\rm f}$ of one or two stellar radii as set by the creation of the pair formation front, and furthermore leads

Table 2
Inferred Best-fit Model LC Parameters for PSR J0034−0534, PSR J1939+2134, and PSR J1959+2048

Model	α	ζ	$r^{\gamma}_{\rm OVC,min}$	$r^{\gamma}_{\rm OVC,max}$	$r^{r}_{\rm OVC,max}$	$r^{r}_{\rm OVC,max}$	$R^{\gamma}_{\rm min}$	$R^{\gamma}_{\rm max}$	$R^{r}_{\rm min}$	$R^{r}_{\rm max}$	f_{Ω}	$-\Delta\ln$(like)
						PSR J0034−0534						
alOG	12^{+40}_{-6}	69^{+10}_{-2}	1.00	1.00	1.00	1.00	$R_{\rm NCS}$	$0.9^{+0.3}_{-0.1}$	$0.2^{+0.6}_{-0.06}$ [a]	$1.1^{+0.1}_{-0.4}$	$0.31^{+0.31}_{-0.04}$	96.1
alTPC	30^{+9}_{-7}	70 ± 2	0.95	1.00	0.90	1.00	$R_{\rm NS}$	0.9 ± 0.1	$0.7^{+0.2}_{-0.3}$	$0.8^{+0.4}_{-0.1}$	$0.62^{+0.15}_{-0.04}$	87.0
laSG1[b]	10	34	0.90	0.95	0.90	0.95	...	...	...	...	0.30	97.3
laSG2[c]	10	37	0.90	0.95	0.90	0.95	...	...	...	...	0.37	98.7
						PSR J1939+2134						
alOG	84^{+2}_{-6}	84^{+1}_{-3}	0.95	0.95	1.00	1.00	$R_{\rm NCS}$	$1.0^{+0.2}_{-0.1}$	0.6 ± 0.1	0.9 ± 0.1	$0.98^{+0.05}_{-0.02}$	130.9
alTPC	75^{+8}_{-6}	80^{+1}_{-3}	0.90	1.00	1.00	1.00	$R_{\rm NS}$	1.0 ± 0.2	$0.7^{+0.1}_{-0.3}$	$0.9^{+0.2}_{-0.1}$	$1.00^{+0.08}_{-0.03}$	126.3
laSG1	30	32	0.90	0.95	0.90	0.95	...	...	...	...	1.06	146.9
laSG2	35	25	0.90	0.95	0.90	0.95	...	...	...	...	0.93	154.6
						PSR J1959+2048						
alOG	31^{+39}_{-3}	89^{+5}_{-3}	0.95	0.95	0.90	0.90	$R_{\rm NCS}$	$1.1^{+0.1}_{-0.2}$	0.7 ± 0.1	$0.9^{+0.2}_{-0.1}$	$0.56^{+0.}_{-0.}$	128.3
alTPC	47^{+5}_{-13}	85^{+1}_{-7}	0.95	1.00	0.95	1.00	$R_{\rm NS}$	$1.2^{+0.1}_{-0.4}$	0.8 ± 0.1	$1.0^{+0.2}_{-0.1}$	$0.82^{+0.06}_{-0.12}$	123.7
laSG1	20	43	0.90	0.95	0.90	0.95	...	...	...	...	0.86	129.0
laSG2	25	45	0.90	0.95	0.90	0.95	...	...	...	...	1.14	141.7

Notes. The columns represent the geometric model (altitude-limited OG (alOG), altitude-limited TPC (alTPC), or low-altitude (laSG) geometry) used for the fit, inclination angle α, observer angle ζ, gamma-ray emission layer width inner boundary $r^{\gamma}_{\rm OVC,min}$, gamma-ray emission layer outer boundary $r^{\gamma}_{\rm OVC,max}$, radio emission layer inner boundary $r^{r}_{\rm OVC,min}$, radio emission layer outer boundary $r^{r}_{\rm OVC,max}$, minimum gamma-ray altitude $R^{\gamma}_{\rm min}$, maximum gamma-ray altitude $R^{\gamma}_{\rm max}$, minimum radio altitude $R^{r}_{\rm min}$, maximum radio altitude $R^{r}_{\rm max}$, geometric factor f_{Ω}, as well as the likelihood of the fit. The angles are in degrees, the altitudes are in units of $R_{\rm LC}$, and the emission layer boundaries are in OVC coordinates which range from 0 to 1 from the magnetic axis to the last open B-field line (as measured on the stellar surface).

[a] This relatively small error reflects the fact that this pulsar's surface is at $\approx 0.14\ R_{\rm LC}$.

[b] An laSG model with $s_{\rm f} = 1.2\ R$, $\sigma_{\rm in} = 0.1\ R$, and $\sigma_{\rm out} = 0.3\ R$.

[c] An laSG model with $s_{\rm f} = 1.5\ R$, $\sigma_{\rm in} = 0.2\ R$, and $\sigma_{\rm out} = 0.5\ R$.

us to choose $r_{\rm OVC,min} = 0.90$ and $r_{\rm OVC,min} = 0.95$, because the gamma-ray photons are mostly created by synchrotron radiation from secondaries interior to the outer boundary of the gap in this model, and not by curvature radiation from the primaries as in the standard SG model. This is similar to what occurs in the OG, where an emission layer develops, touching the inner gap boundary.

The laSG models have five free parameters (excluding P): (α, ζ, $s_{\rm f}$, $\sigma_{\rm in}$, $\sigma_{\rm out}$), since we use the same values for the emission layer boundaries of both the radio and gamma-ray emission regions, and keep them fixed as explained above, resulting in an emission layer width $w = 5\%$. If needed, the latter may be freed, resulting in either seven free parameters in total, or nine if one chooses to uncouple the gamma-ray and radio emission boundaries. In what follows, we disregard LC fits from the constant-emissivity laSG models, as these models cannot reproduce the sharp peaks seen in the gamma-ray and radio data (see Figures 14–23).

4. AN MCMC TECHNIQUE FOR FINDING OPTIMAL LC FITS IN MULTIVARIATE PARAMETER SPACE

In order to statistically pick the best-fit parameters, for the alOG and alTPC models and for the three MSPs considered here, we have developed an MCMC maximum likelihood procedure (more details will be given in T. J. Johnson et al. 2011, in preparation). The gamma-ray LCs are fit using Poisson likelihood while the radio LCs are fit using a χ^2 statistic and the two values are combined. For a given parameter state the likelihood value is calculated by independently optimizing the radio and gamma-ray model normalizations using the *scipy* python module[6] and the *scipy.optimize.fmin_l_fbgs_b* multivariate, bound optimizer (Zhu et al. 1997). An MCMC involves taking random steps in parameter space and accepting a step based on the likelihood ratio with respect to the previous step (Hastings 1970). The likelihood surfaces can be very multimodal which can lead to poor mixing of the chain and slow convergence. Therefore, we have implemented small-world chain steps (Guan et al. 2006) and simulated annealing (Marinari & Parisi 1992) to speed up the convergence and ensure that the MCMC fully explores the parameter space and does not get stuck in a local maximum. We verify that our chains have converged using the criteria proposed by Gelman & Rubin (1992).

In order to balance the gamma-ray and radio contributions to the likelihood, we have chosen to use a radio uncertainty which is equal to the average relative gamma-ray uncertainty in the on-peak region times the maximum radio value. The choice of radio uncertainty can strongly affect the best-fit results; in particular, a smaller uncertainty will decrease the overall likelihood and can, in some cases, lead to a different best-fit geometry which favors the radio LC more strongly. When varying the radio uncertainty by a factor of two, the best-fit α and ζ values of PSR J0034−0534 were found to change by $\lesssim 13^{\circ}$. For PSR J1939+2134, the best-fit α and ζ were found to vary by $\leqslant 7^{\circ}$ when varying the radio uncertainty. The best-fit geometry of PSR J1959+2048 was found to be the most sensitive to changes in the radio uncertainty, with either the best-fit α or ζ value changing by $\sim 35^{\circ}$, while the other parameter changed by $\lesssim 15^{\circ}$.

[6] See http://docs.scipy.org/doc/ for documentation.

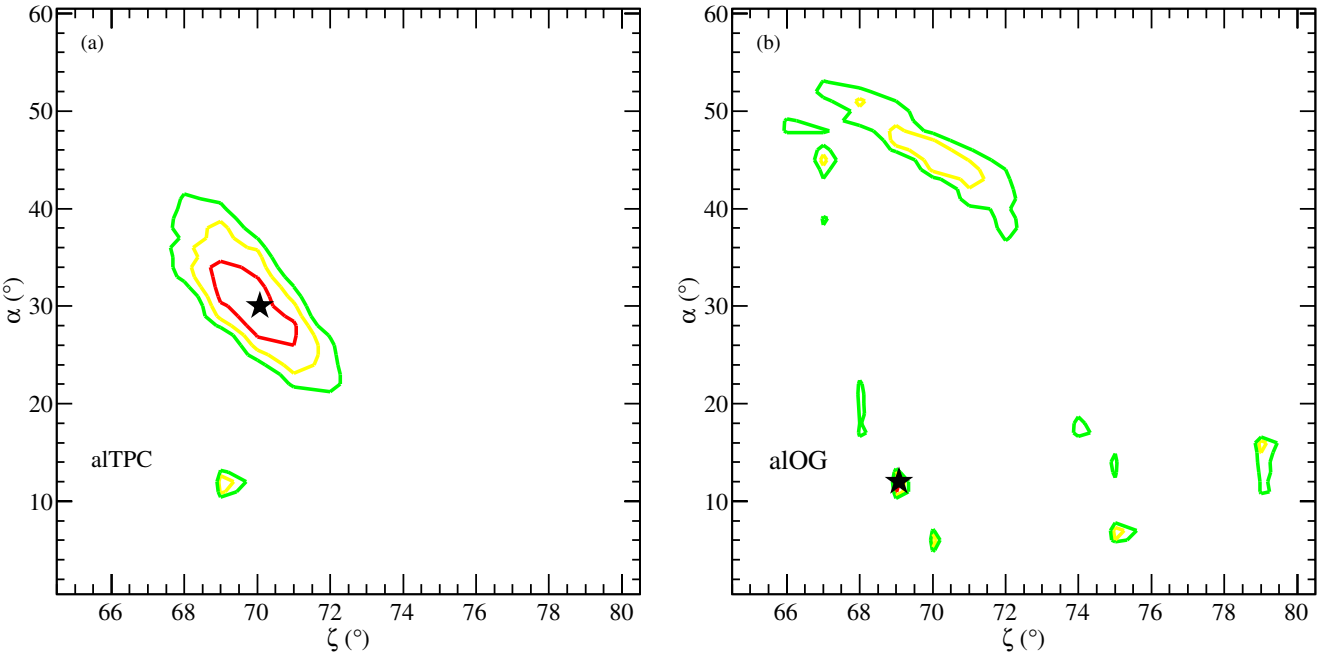

Figure 2. Plots of $(-\Delta \ln(\text{likelihood}))$ vs. α and ζ for PSR J0034−0534. The contours mean the following: light gray (red online) is 68%, dark gray (yellow online) 95%, and black (green online) is 99%. The left panel is for the alTPC model, while the right panel is for the alOG model. The best-fit geometries are indicated by the black stars.

(A color version of this figure is available in the online journal.)

Our simulations have a resolution of 1° in both α and ζ, 0.05 in both $r_{\rm OVC,min}$ and $r_{\rm OVC,max}$, and $0.1R_{\rm LC}$ for the minimum and maximum emission altitudes $R_{\rm min}$ and $R_{\rm max}$. The available values of $r_{\rm OVC,min}$ and $r_{\rm OVC,max}$ lead to possible values of w of 0.00, 0.05, or 0.10. The MCMC only explores α from 1° to 90° and ζ from 0° to 89°, as going beyond this range produces the same profiles simply shifted in phase by 180°. Additionally, for the gamma-ray models we restrict the maximum emission altitudes to be $R^{\gamma}_{\rm max} \geqslant 0.70R_{\rm LC}$. For the alTPC and alOG models the simulations were generated with a spin period of 1.5 ms which puts the NS surface at $R_{\rm NS} = 0.14R_{\rm LC}$. In addition to predicting the best-fit model parameters, the simulations also provide numerical estimates of the beaming correction factor (f_Ω) as described in Venter et al. (2009). The quantity f_Ω is the ratio of the total flux over the sky for the best-fit α (for all ζ) to the phase-averaged observed flux at the best-fit α and ζ (Watters et al. 2009).

The chains were run until they had a total of 200,000 accepted steps (typically running eight chains of 25,000 steps each) in order to guarantee convergence. Starting from the best-fit parameters found by the MCMC, we then produced confidence contours in α and ζ by performing likelihood profile scans over the other parameters, allowing for the possibility of finding a better fit. Figures 2–4 show these contours for PSR J0034−0534, PSR J1939+2134, and PSR J1959+2048. The uncertainties on α and ζ quoted in Table 2 are approximate 95% confidence level uncertainties. When comparing the inferred α and ζ to those found using observations at other wavelengths (such as radio polarization measurements), our (α, ζ) contours should rather be used to assess the true significance of our best-fit values, as the contours indicate the actual uncertainties encapsulated by the estimated linear error bars given in Table 2. For example, the confidence contours corresponding to the alOG fit of PSR J0034−0534 consist of several small and disjointed clusters. As such, we cannot confidently constrain the geometry well in this case and thus report uncertainties in Table 2 that cover the entire contour region.

We can also estimate uncertainties on the emission altitude parameters using the information from the likelihood profile scans which generated the confidence contours. An example is shown in Figure 5. The estimated 95% uncertainties from the likelihood profile are given in Table 2 as well.

For each (α, ζ) pair within the 95% contours, the beaming correction factor $f_\Omega(\alpha, \zeta)$ is estimated; these values are then used to provide the confidence intervals for f_Ω given in Table 2. Uncertainties in the other model parameters were found to have less impact on f_Ω.

We have not yet implemented an MCMC for the laSG models. The manually selected and MCMC-selected LC fits agree very well for several MSPs for which both methods have been applied. The MCMC contour plots of the likelihood will be evolving as more data are accumulated and the relative errors are decreased (especially in the gamma-ray band). Manual fits may overemphasize the gamma-ray profiles, given the very small errors of the radio profiles. Also, the latter lacks the mathematical rigor of a statistically driven fitting procedure. In order to more directly compare the laSG and the alOG/alTPC fits we have used the same method to calculate the laSG model normalizations as that used in the maximum likelihood code. This allows us to find the normalizations that give the best likelihood value for a given set of laSG model parameters. As the parameter space has not been fully explored we do not claim that this represents the maximum likelihood for the laSG models and thus no claim can be made as to whether or not laSG models are preferred for the three MSPs modeled here.

5. RESULTS

Below we discuss the effect of letting $R_{\rm min}$ and $R_{\rm max}$ be free parameters in the alOG/alTPC model context for both the radio and gamma-ray emission regions. Similarly, we

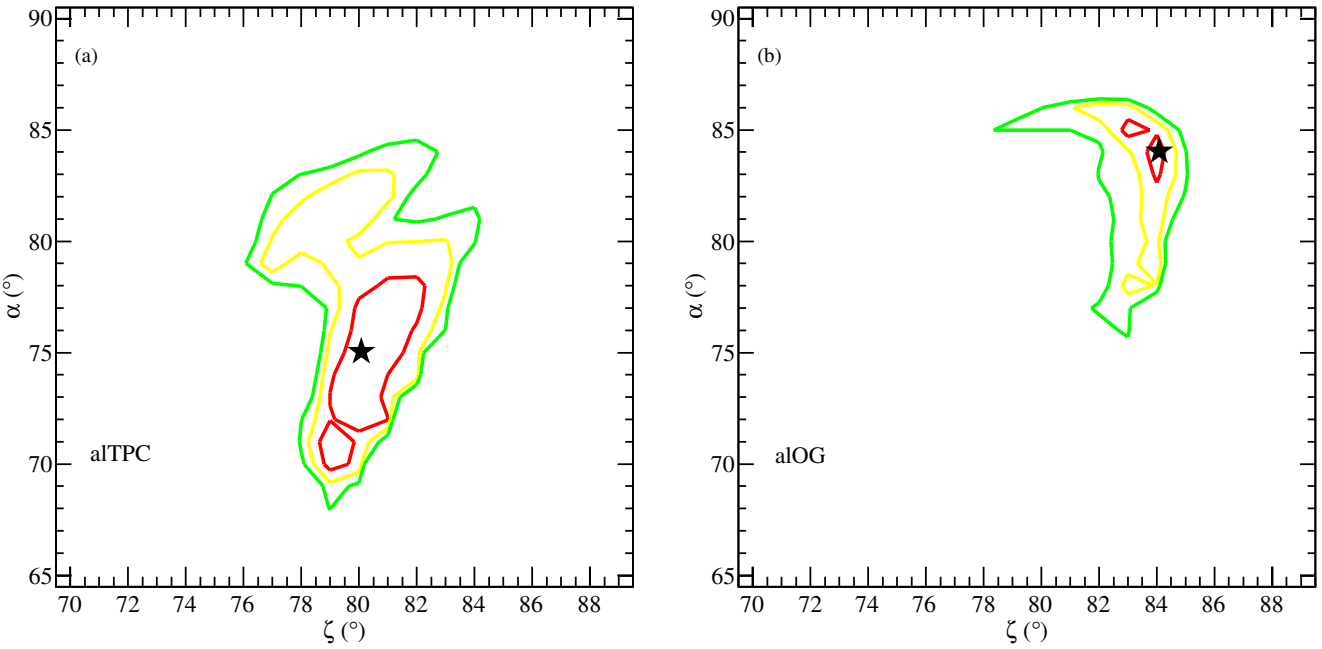

Figure 3. Same as Figure 2, but for PSR J1939+2134.
(A color version of this figure is available in the online journal.)

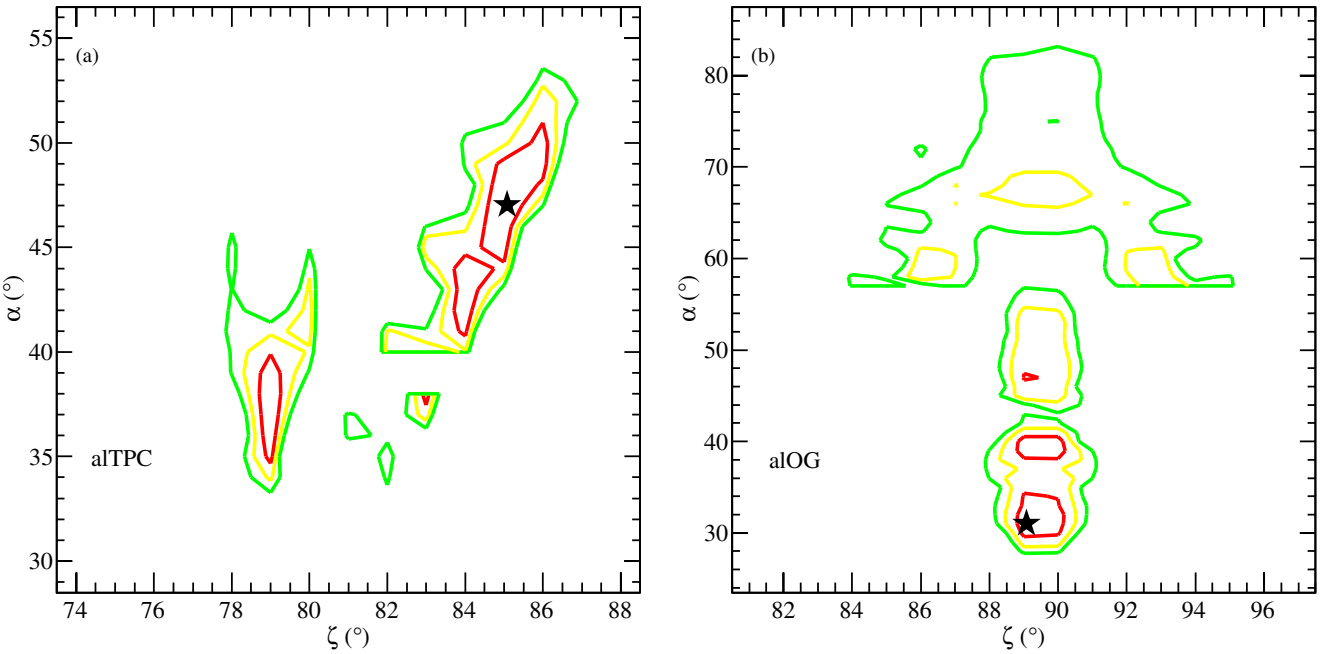

Figure 4. Same as Figure 2, but for PSR J1959+2048.
(A color version of this figure is available in the online journal.)

discuss the effect of using different fading parameters in our laSG models. For each class of models, we also describe the results of our LC fits to PSR J0034−0534, PSR J1939+2134, and PSR J1959+2048. See Table 2 as well as figure captions of individual pulsar LC fits for the parameters α, ζ, $R^{\gamma}_{\rm min}$, $R^{\gamma}_{\rm max}$, $R^{r}_{\rm min}$, $R^{r}_{\rm max}$, $r^{\gamma}_{\rm OVC,min}$, $r^{\gamma}_{\rm OVC,max}$, $r^{r}_{\rm OVC,min}$, $r^{r}_{\rm OVC,max}$, $s_{\rm f}$, $\sigma_{\rm in}$, $\sigma_{\rm out}$, and f_{Ω} inferred/assumed for each of these MSPs in the context of the different models.

5.1. The alOG and alTPC Models

Figures 6–9 show the effect of increasing $R_{\rm min}$ while keeping $R_{\rm max}$ constant for $(\alpha, \zeta) = (30^{\circ}, 70^{\circ})$ and $(\alpha, \zeta) = (65^{\circ}, 80^{\circ})$ for an alTPC and an alOG model, respectively.[7] We used $R_{\rm min} = (0.12, 0.40, 0.70)R_{\rm LC}$ for the different panels (where the stellar radius $R_{\rm NS} \approx 0.12R_{\rm LC}$ for $P = 1.877$ ms), while setting $R_{\rm max} = 1.20R_{\rm LC}$. Neglecting low-altitude emission is roughly equivalent to growing the PC size (i.e., deleting a ring of radiation around the PC in the phaseplot), as may be seen in panels (a)–(c) in each case. This has the effect that low-level off-peak emission is suppressed in the corresponding LCs

[7] Note that the phaseplots indicate *relative* intensity per solid angle versus ζ and ϕ, and have different color scales for each instance (parameter combination). The visualization is done in such a way as to enhance the structural details of the projected emission pattern. Therefore, different phaseplots should only be compared qualitatively.

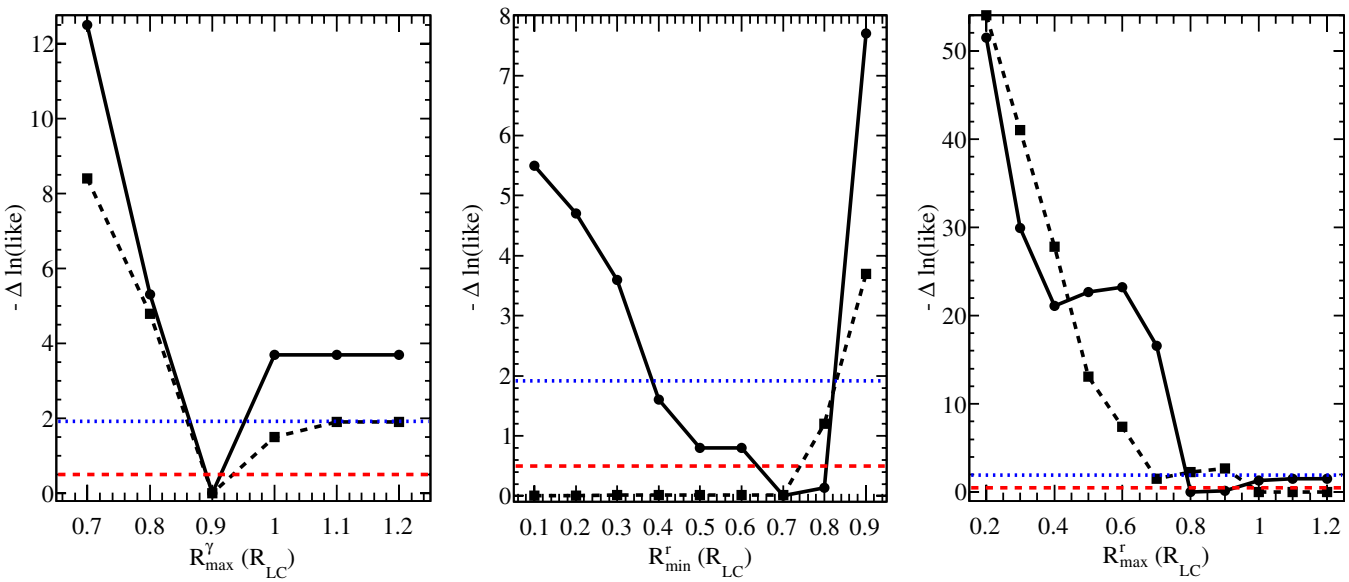

Figure 5. Plots of the likelihood vs. various emission altitudes for PSR J0034−0534, with the solid lines indicating the alTPC model, while the dashed lines are for the alOG model. The horizontal long-dashed (red online) and fine-dashed (blue online) lines indicate the 1σ and 2σ errors, respectively.
(A color version of this figure is available in the online journal.)

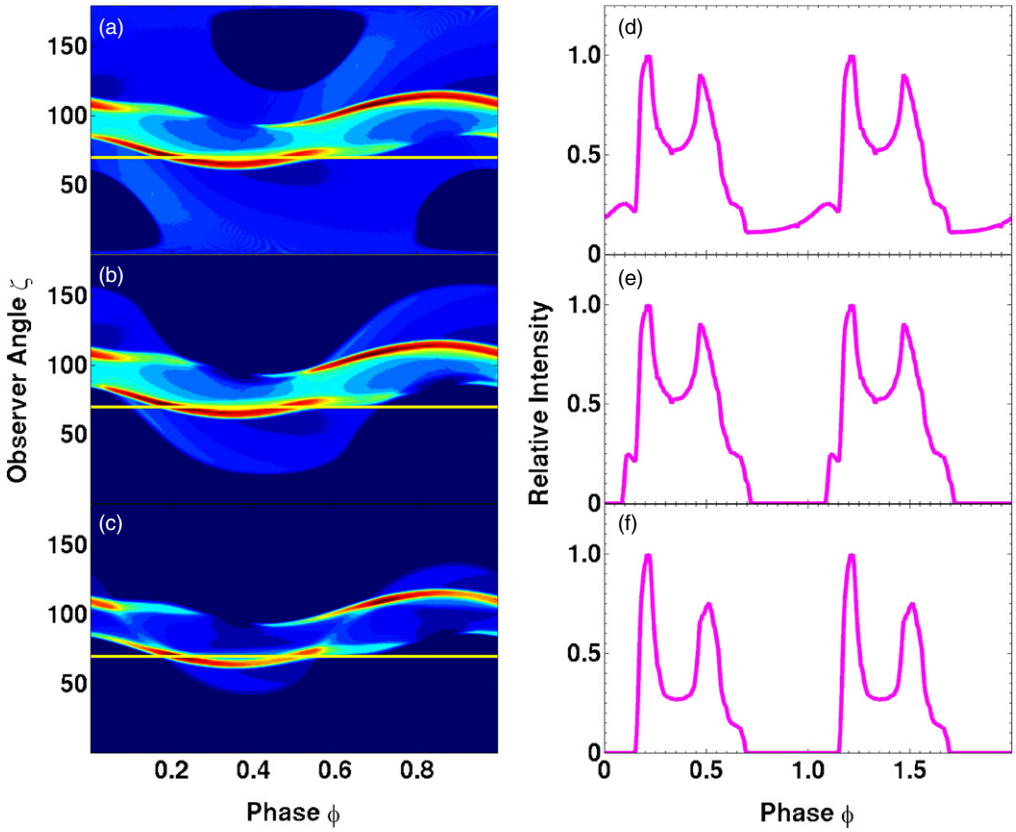

Figure 6. Phaseplots (left column; 1 rotation) and LCs (right column; 2 rotations, with $\zeta = 70^{\circ}$) of an alTPC model showing the effect of increasing $R_{\rm min}$ and keeping $R_{\rm max}$ fixed. Panels (a) and (d): $R_{\rm min} = 0.12R_{\rm LC} \approx R_{\rm NS}$; panels (b) and (e): $R_{\rm min} = 0.40R_{\rm LC}$; panels (c) and (f): $R_{\rm min} = 0.70R_{\rm LC}$. We used $\alpha = 30^{\circ}$, $r_{\rm OVC,min} = 0.95$, $r_{\rm OVC,max} = 1.00$, $P = 1.877$ ms, and $R_{\rm max} = 1.20R_{\rm LC}$.
(A color version of this figure is available in the online journal.)

(especially for the alTPC case) for both interpulse ("wing") emission between two consecutive profiles (e.g., Figure 6(f)) and interpeak ("bridge") emission (e.g., Figure 7(f)), depending on α and ζ. The peaks therefore become sharper. This is a smaller effect in the case of the alOG models, as these do not have emission from below the NCS, and off-peak emission of standard OG LCs is usually inhibited to start with (compare Figure 6(d) with Figure 8(d)). Comparison of the phaseplots of alOG versus alTPC models reveals that much of the off-peak emission originates from below the NCS (e.g., Figure 7(a)

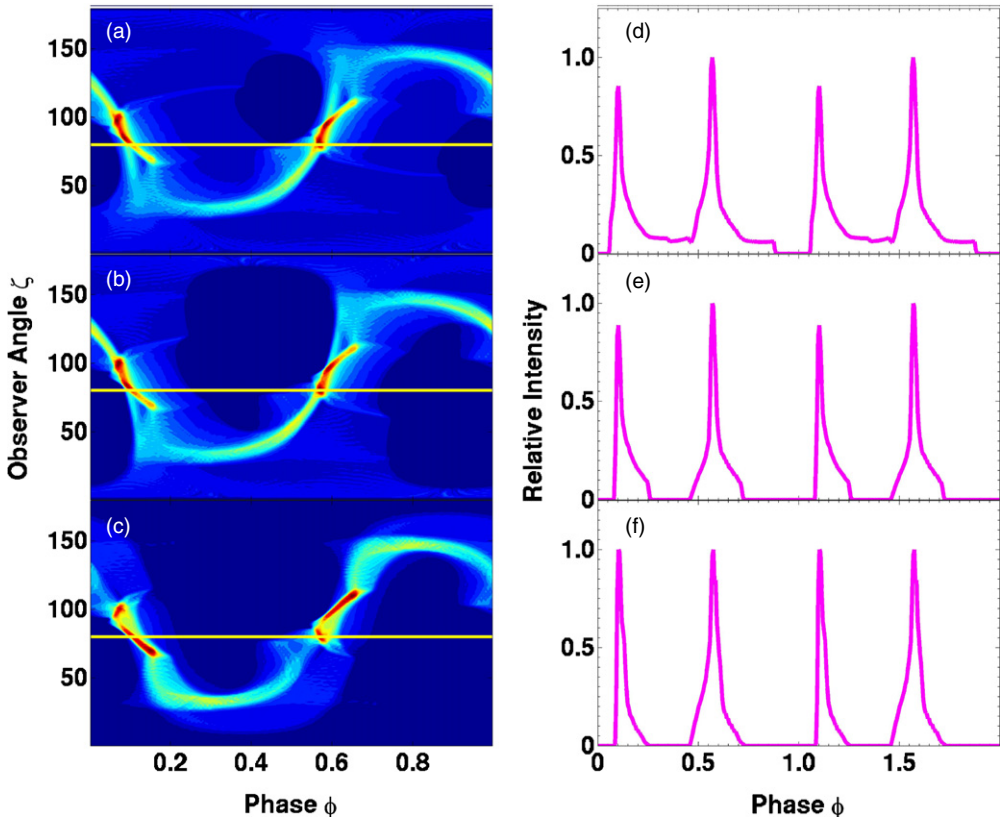

Figure 7. Same as Figure 6, but for $\alpha = 65^\circ$ and $\zeta = 80^\circ$.
(A color version of this figure is available in the online journal.)

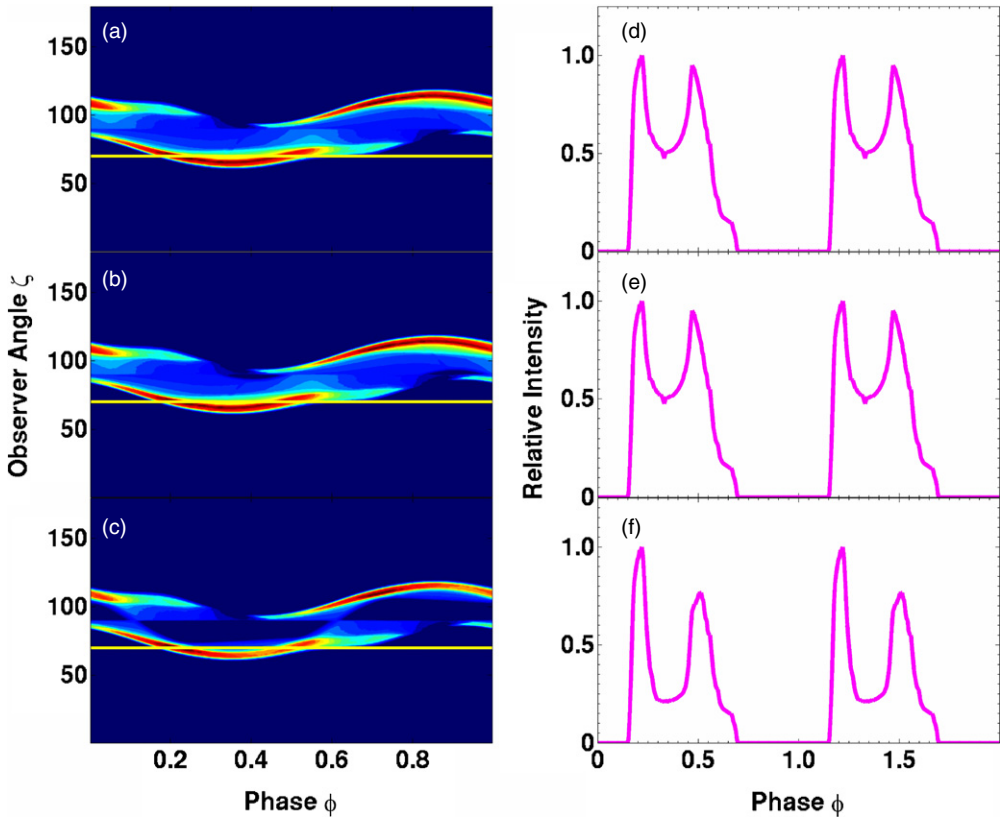

Figure 8. Phaseplots (left column) and LCs (right column, with $\zeta = 70^\circ$) of an alOG model showing the effect of increasing $R_{\rm min}$ and keeping $R_{\rm max}$ fixed. Panels (a) and (d): $R_{\rm min} = \max\{0.12R_{\rm LC}, R_{\rm NCS}\}$; panels (b) and (e): $R_{\rm min} = \max\{0.40R_{\rm LC}, R_{\rm NCS}\}$; panels (c) and (f): $R_{\rm min} = \max\{0.70R_{\rm LC}, R_{\rm NCS}\}$. We used $\alpha = 30^\circ$, $r_{\rm OVC,min} = 0.95$, $r_{\rm OVC,max} = 1.00$, $P = 1.877$ ms, and $R_{\rm max} = 1.20R_{\rm LC}$.
(A color version of this figure is available in the online journal.)

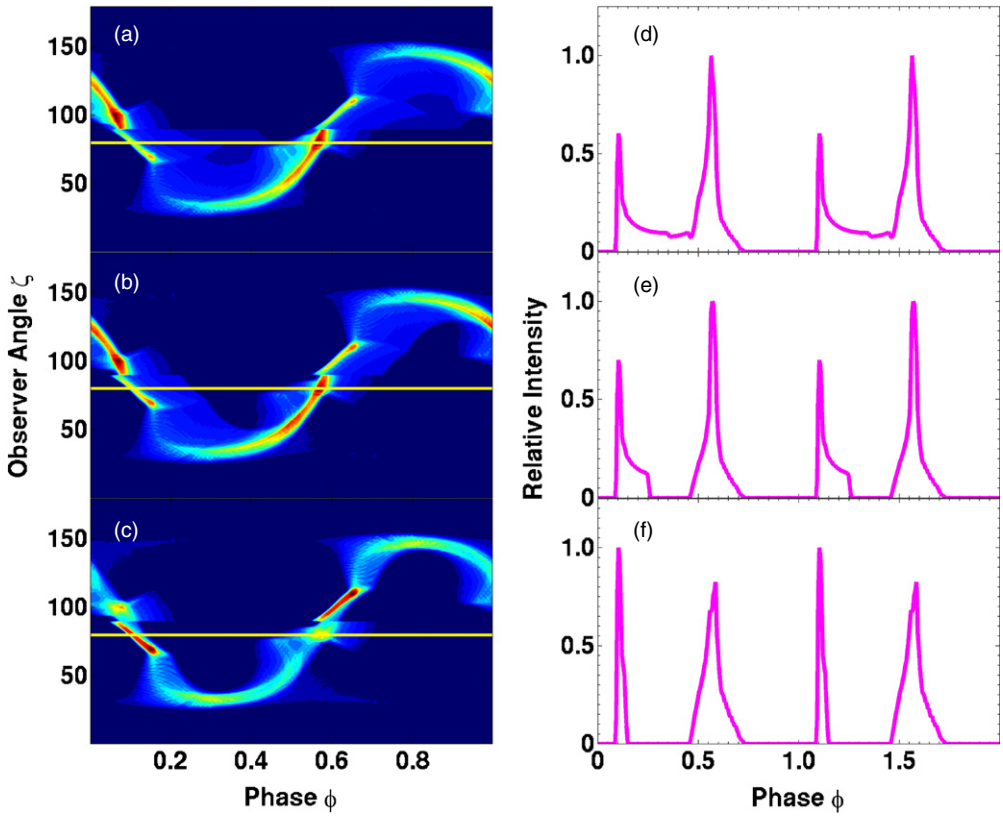

Figure 9. Same as Figure 8, but for $\alpha = 65^\circ$ and $\zeta = 80^\circ$.
(A color version of this figure is available in the online journal.)

versus Figure 9(a)). This implies that the NCS must in some cases be quite high, as there is a difference between the alOG and alTPC phaseplots even for $R_{\rm min} > 0.70R_{\rm LC}$. In the case of higher inclinations, the leading peak of the alOG LC is significantly lower than that of the alTPC LC when the low-altitude emission is included. This is due to the absence of caustic emission coming from low altitudes from the second pole, as alOG models are effectively one-pole caustic models.

Figures 10–13 indicate the effect of decreasing $R_{\rm max}$ while keeping $R_{\rm min}$ constant, again for $(\alpha, \zeta) = (30^\circ, 70^\circ)$ and $(\alpha, \zeta) = (65^\circ, 80^\circ)$, and for both alTPC and alOG models. We used $R_{\rm max} = (1.20, 0.80, 0.60)R_{\rm LC}$, while setting $R_{\rm min} = 0.12R_{\rm LC} \approx R_{\rm NS}$ for the alTPC, and $R_{\rm min} = R_{\rm NCS}$ for the alOG model. Decreasing $R_{\rm max}$ has the effect of constraining the emission to a ring-like structure around the PC (reminiscent of a hollow cone in the low-altitude TPC or laSG case). As a result, the relative peak heights change in the corresponding LCs and low-level features may become more prominent. For small α values (e.g., Figures 10(f) and 12(f)), off-peak emission is eroded and both caustic peaks even disappear for a small enough value of $R_{\rm max}$. The caustic peaks become sharper for larger α with decreasing $R_{\rm max}$ (e.g., Figures 11(f) and 13(f)). For high α, the leading peak disappears altogether in the alOG model when excluding too much high-altitude emission (see Figure 13(f)), since it is a caustic formed by overlapping field lines very near $R_{\rm LC}$. Again, the low-altitude emission in the alTPC model yields significant off-peak emission, absent from the alOG model, and this is particularly evident for a substantially decreased value of $R_{\rm max}$.

LC fits for PSR J0034−0534 are shown in Figure 14 (best-fit parameters for the LCs of all MSPs are summarized in Table 2). We found that including high-altitude emission (increasing $R_{\rm max}$) boosts the intensity of the leading gamma-ray peak, while broadening and also boosting the second one. The leading gamma-ray peak's sharpness and intensity also strongly depends on inclusion of emission below $\sim 0.7R_{\rm LC}$. Note that the 0 of the data is the radio phase, while the 0 of the model is the phase of the magnetic pole. We therefore introduce a phase shift $\phi_0 = -0.27$ for all profiles (i.e., we shifted *both* gamma-ray and radio model LCs by ϕ_0 to align them to the data) and use a gamma-ray background of nine events, a relative radio background of 0.08, and 30 bins for both the gamma-ray and radio profiles. The best-fit emission altitudes are given in Table 2. Our results are still close to those cited in Abdo et al. (2010b), who used 13 months of data, while our data span 16 months. The inferred alTPC angles are the same, $(\alpha, \zeta) = (30^\circ, 70^\circ)$, while we now find a slightly different geometry for the alOG model (previously $(\alpha, \zeta) = (30^\circ, 70^\circ)$, now $(\alpha, \zeta) = (12^\circ, 69^\circ)$). Also, the gamma-ray emission layer extent remains the same, while the alTPC radio extent is close (ours being $(R^r_{\rm min}, R^r_{\rm max}) = (0.7, 0.8)R_{\rm LC}$ versus their $(R^r_{\rm min}, R^r_{\rm max}) = (0.6, 0.8)R_{\rm LC}$), but the alOG's is now much larger ($(R^r_{\rm min}, R^r_{\rm max}) = (0.2, 1.1)R_{\rm LC}$ versus the previous $(R^r_{\rm min}, R^r_{\rm max}) = (0.6, 0.8)R_{\rm LC}$).

The alOG/alTPC LC fits for PSR J1939+2134 are shown in Figure 15. We used $\phi_0 = 0.07$, a gamma-ray background of 191.3 events, relative radio background of 0.007, and 30 bins for both the gamma-ray and radio profiles. Although the models reproduce the two main gamma-ray peaks reasonably well, they both miss the feature at phase ~ 0.3; on the other hand, the radio LCs manage to reproduce the correct peak positions and heights. Figure 16 indicates the alOG/alTPC LC fits for PSR J1959+2048. Here, we used $\phi_0 = 0.07$ for the radio and

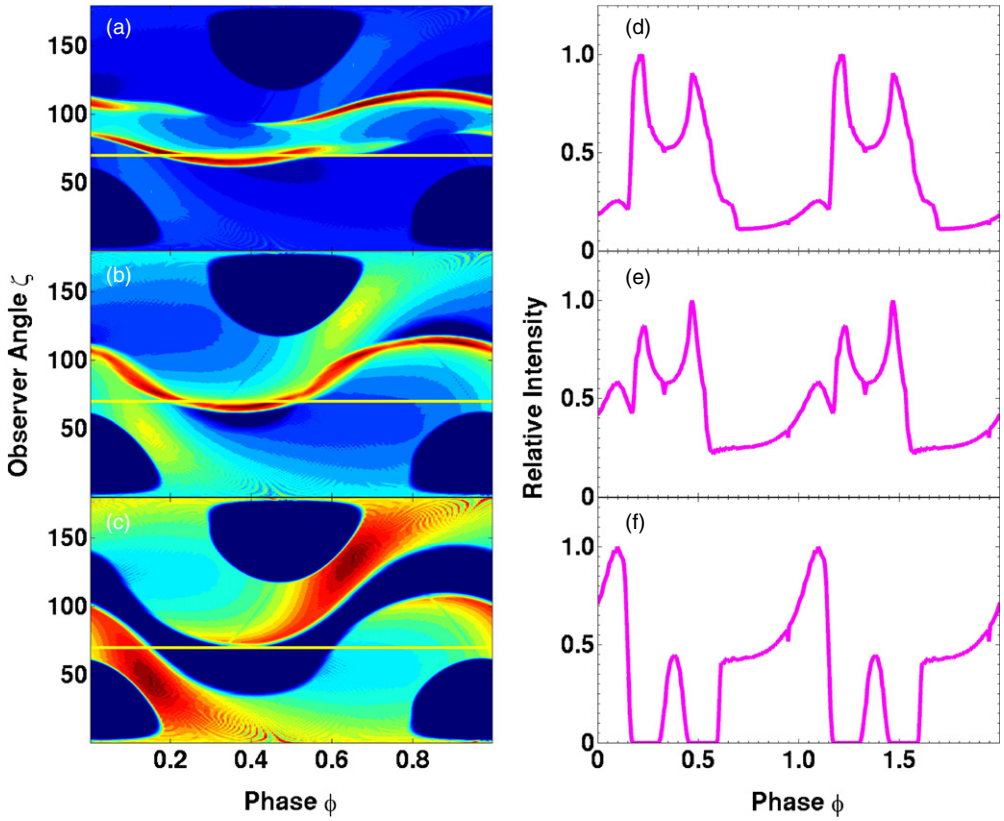

Figure 10. Phaseplots (left column) and LCs (right column, with $\zeta = 70^\circ$) of an alTPC model showing the effect of decreasing $R_{\rm max}$ and keeping $R_{\rm min}$ fixed. Panels (a) and (d): $R_{\rm max} = 1.20R_{\rm LC}$; panels (b) and (e): $R_{\rm max} = 0.80R_{\rm LC}$; panels (c) and (f): $R_{\rm max} = 0.60R_{\rm LC}$. We used $\alpha = 30^\circ$, $r_{\rm OVC,min} = 0.95$, $r_{\rm OVC,max} = 1.00$, $P = 1.877$ ms, and $R_{\rm min} = 0.12R_{\rm LC} \approx R_{\rm NS}$.

(A color version of this figure is available in the online journal.)

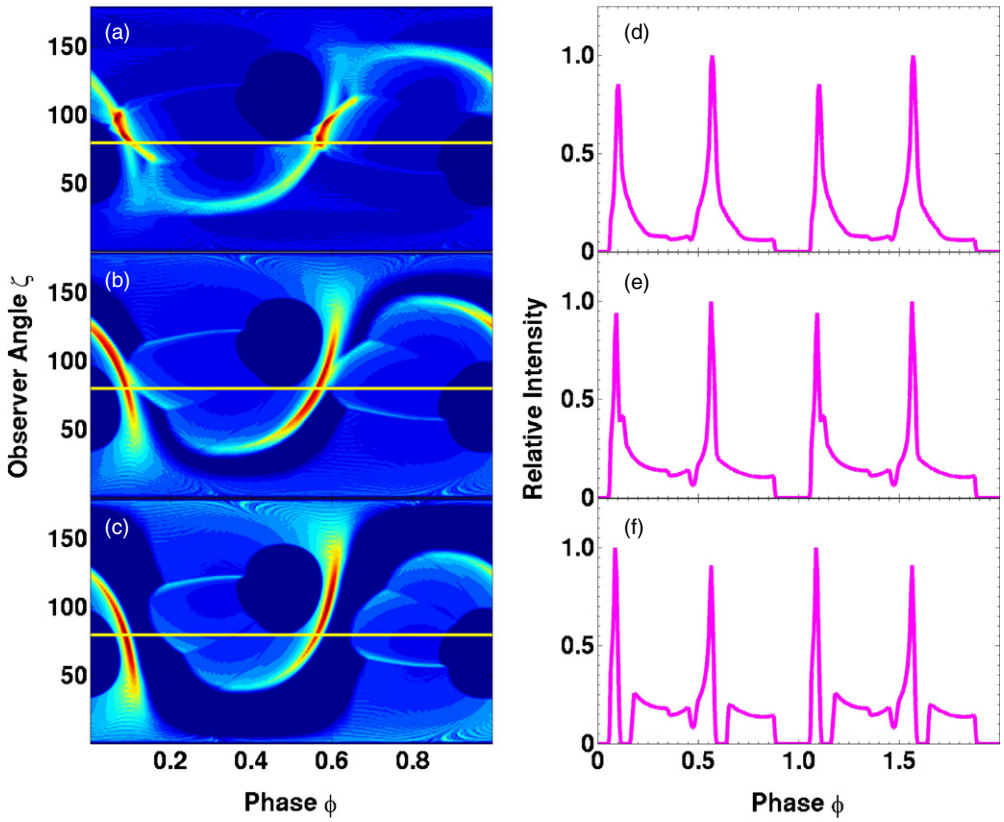

Figure 11. Same as Figure 10, but for $\alpha = 65^\circ$ and $\zeta = 80^\circ$.

(A color version of this figure is available in the online journal.)

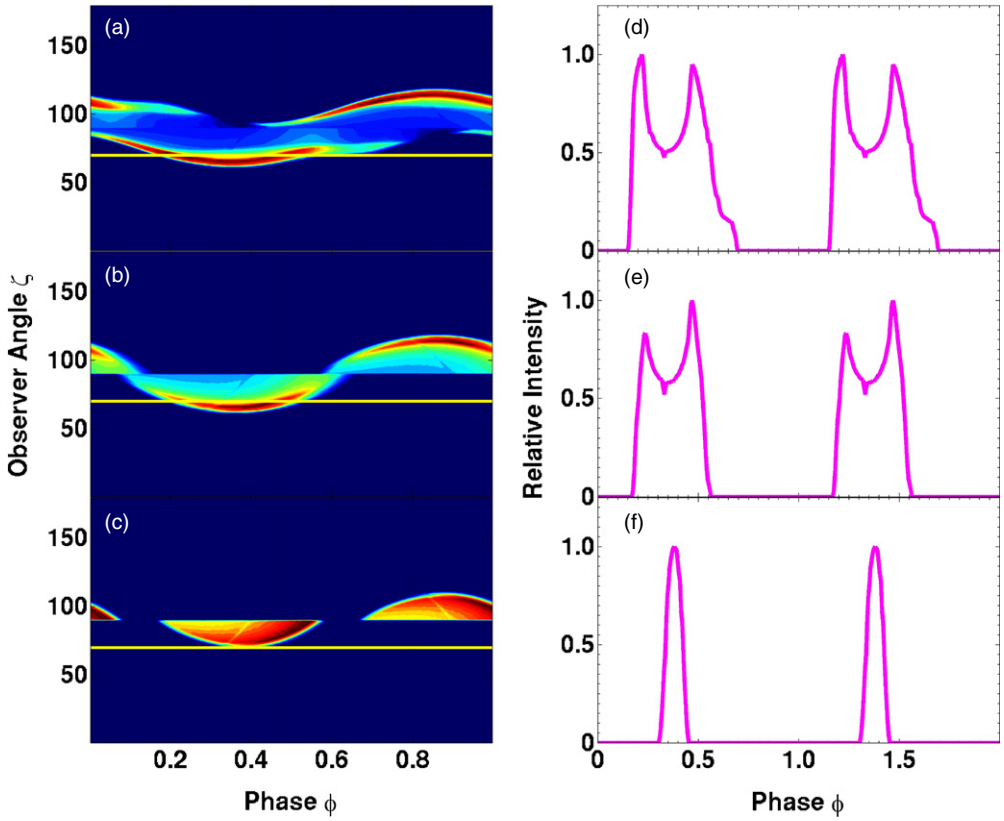

Figure 12. Phaseplots (left column) and LCs (right column, with $\zeta = 70^\circ$) of an alOG model showing the effect of decreasing $R_{\rm max}$ and keeping $R_{\rm min}$ fixed. Panels (a) and (d): $R_{\rm max} = 1.20 R_{\rm LC}$; panels (b) and (e): $R_{\rm max} = 0.80 R_{\rm LC}$; panels (c) and (f): $R_{\rm max} = 0.60 R_{\rm LC}$. We used $\alpha = 30^\circ$, $r_{\rm OVC,min} = 0.95$, $r_{\rm OVC,max} = 1.00$, $P = 1.877$ ms, and $R_{\rm min} = R_{\rm NCS}$.

(A color version of this figure is available in the online journal.)

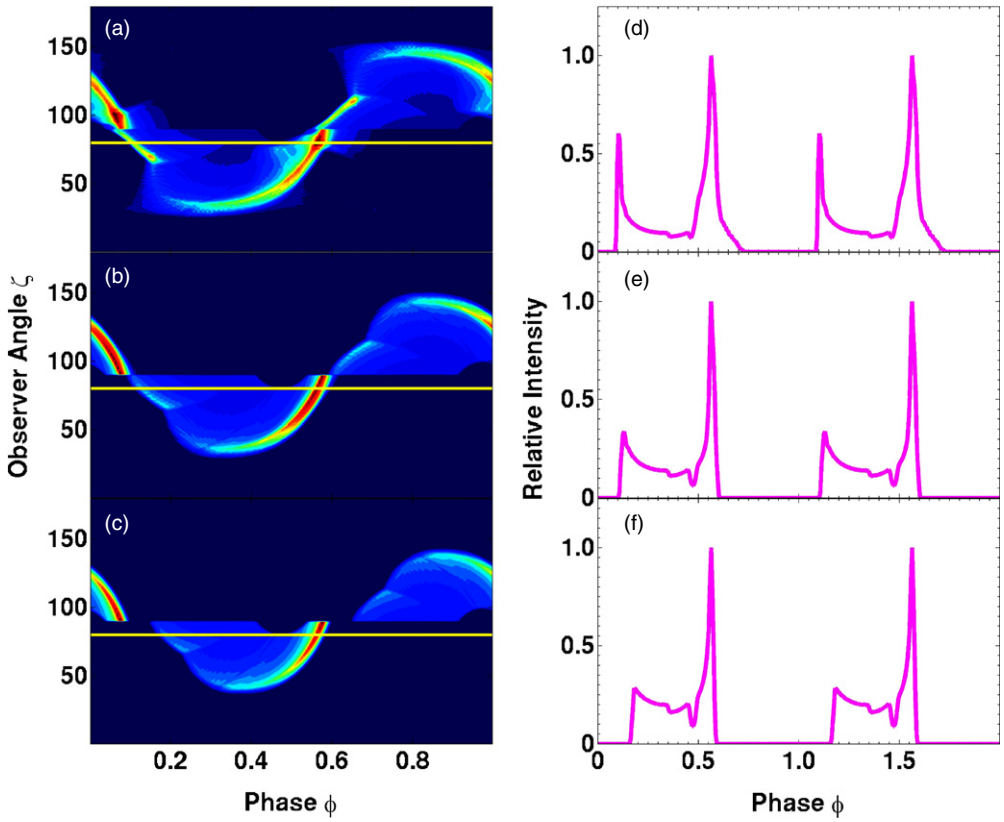

Figure 13. Same as Figure 12, but for $\alpha = 65^\circ$ and $\zeta = 80^\circ$.

(A color version of this figure is available in the online journal.)

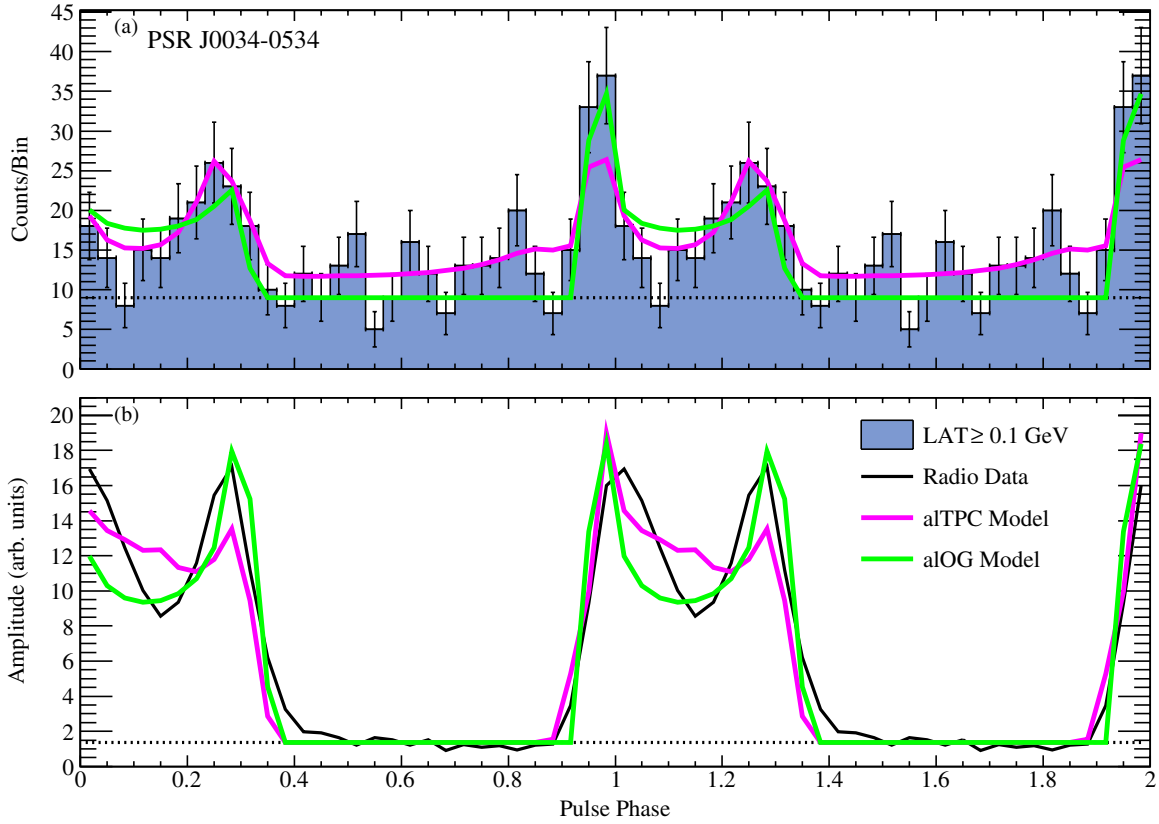

Figure 14. LC fits for PSR J0034−0534 using alTPC/alOG models. Panel (a) shows the gamma-ray data, while panel (b) shows the radio data. Our best-fit parameters are listed in Table 2; also see the text for more details.

(A color version of this figure is available in the online journal.)

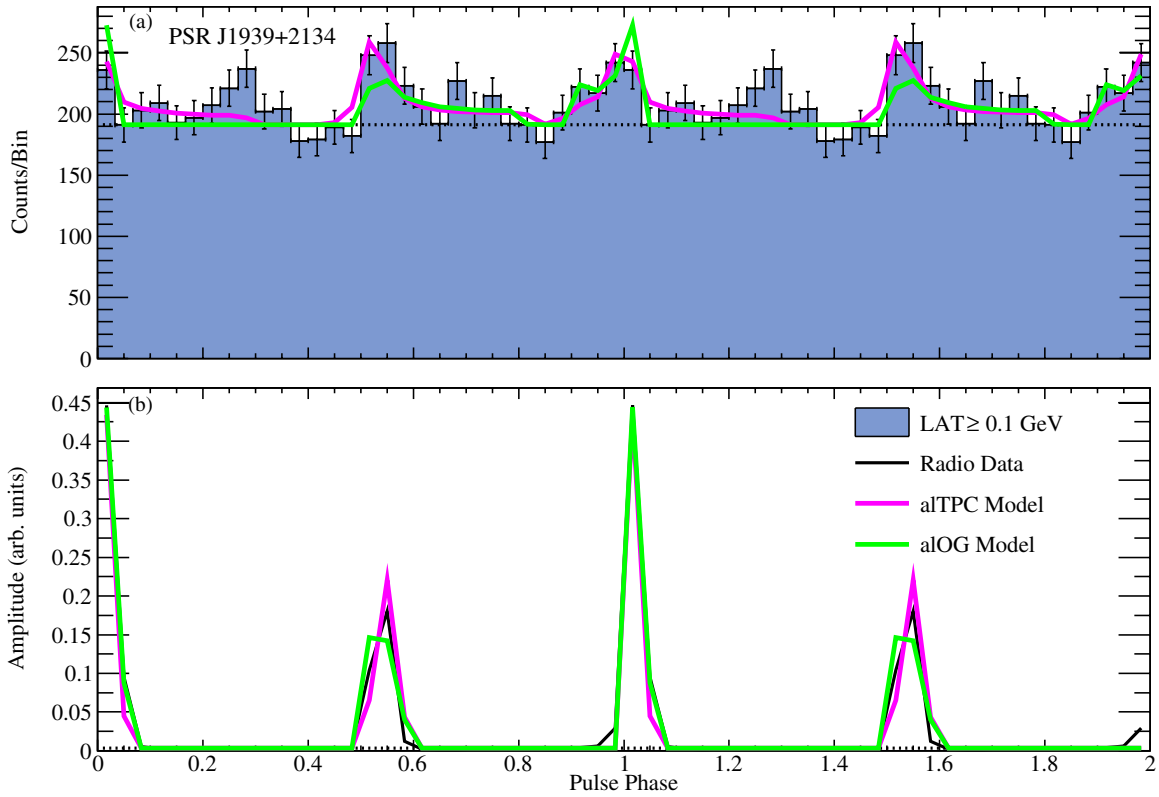

Figure 15. Same as Figure 14, but for PSR J1939+2134.

(A color version of this figure is available in the online journal.)

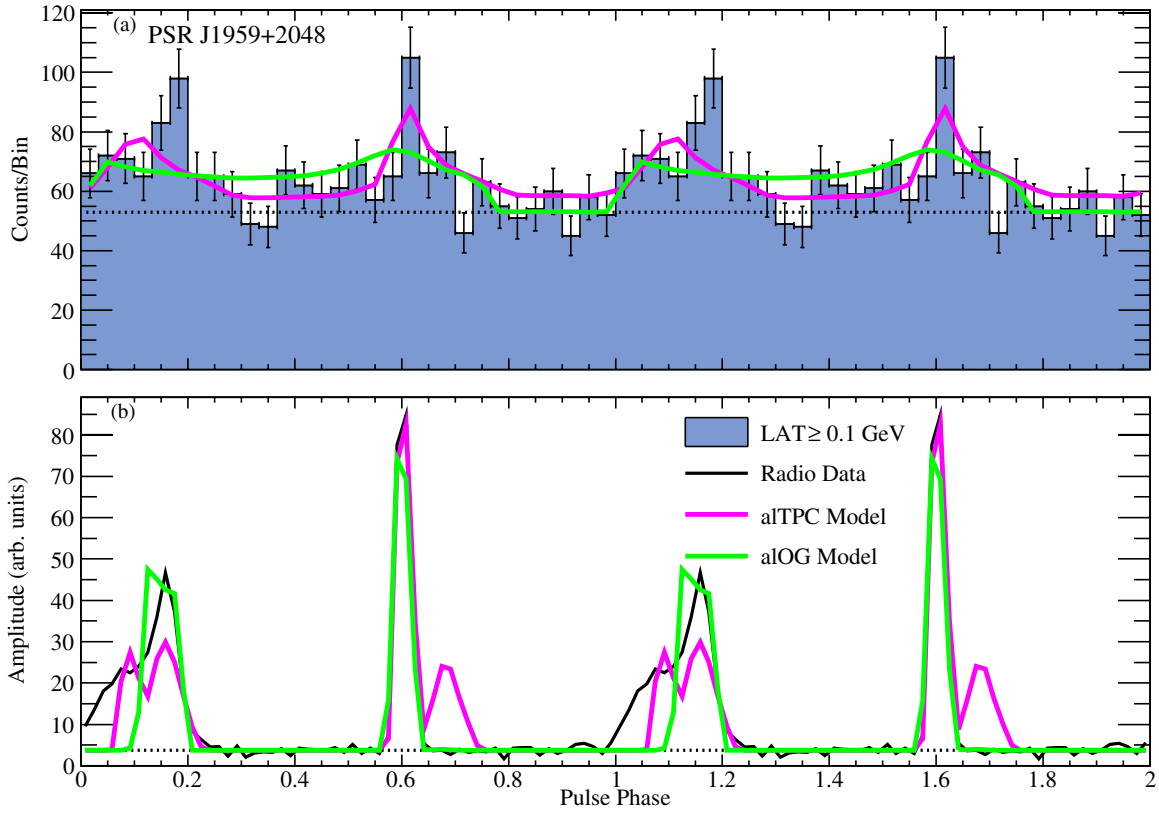

Figure 16. Same as Figure 14, but for PSR J1959+2048.
(A color version of this figure is available in the online journal.)

gamma-ray profiles of the alTPC model, $\phi_0 = 0.47$ for the alOG model, and used a gamma-ray background of 53 events, a relative radio background of 0.05, 30 bins for the gamma-ray profile, and 60 bins for the radio profile. The best-fit geometries are largely driven by the radio profile and in neither case are the narrow gamma-ray peaks well reproduced. This is thought to be a result of the peaks consisting of one or two bins in the LC and, with the current statistics, not influencing the likelihood significantly. With more LAT data the LC and fits should improve. Our LC results are the same as those cited in Guillemot et al. (2012) for these last two pulsars.

5.2. The laSG Models

Figure 17 indicates results from the constant-emissivity laSG model with low-altitude emission. The left column indicates phaseplots, while the right column indicates the corresponding model LCs, as well as the *Fermi* profile for PSR J0034−0534 using the same gamma-ray data span as in Ackermann et al. (2011) and the same timing model described in Abdo et al. (2010b). We used different values for $R_{\rm min}$ and $R_{\rm max}$. In panels (a) and (d), $(R_{\rm min}, R_{\rm max}) = (0.12, 0.20)R_{\rm LC}$; panels (b) and (e), $(R_{\rm min}, R_{\rm max}) = (0.12, 0.40)R_{\rm LC}$; and panels (c) and (f), $(R_{\rm min}, R_{\rm max}) = (0.30, 0.40)R_{\rm LC}$. (Note that the value of $R_{\rm max}$ is not typically so large for the laSG model as used here; we chose these values to emphasize the general behavior of the model. Below, we use more realistic values of one or two stellar radii.) We furthermore used $(\alpha, \zeta) = (30^\circ, 50^\circ)$, $(r_{\rm OVC,min}, r_{\rm OVC,max}) = (0.90, 0.95)$ implying $w = 0.05$, $\phi_0 = 0.15$, $P = 1.877$ ms, and gamma-ray background of 9 events. It is evident that the leading peak is wider while the trailing peak is sharper in each case. This is due to aberration effects leading to caustic emission (Morini 1983) even for this low-altitude emission. Also, by including emission from higher altitudes, the peaks become broader (compare Figures 17(d) and (e)). Lastly, the peak phase separation and width may be altered by choosing different values of $R_{\rm min}$ and $R_{\rm max}$ (Figure 17(f)). Due to the block shape of the resulting peaks, we do not consider this model as a viable contender, but rather introduce modulation of the emissivity profile using fading parameters.

Figures 18–20 indicate the effect of changing the fading parameters $(\sigma_{\rm in}, \sigma_{\rm out}, s_{\rm f})$ for different values of α and ζ. The σ-parameters determine the sharpness of the rise and fall of the emissivity profile (along the B-field), while $s_{\rm f}$ determines the position of the peak emission; again, the effect of brightening of the trailing peak due to caustic effects is apparent as also noted by Dyks et al. (2010). It is clear that peak widths may be fine-tuned using the σ-parameters, while the peak positions are strongly influenced by $s_{\rm f}$. The peak separation depends sensitively on ζ. Generally, the laSG model can produce one, two, three, or four peaks depending on the geometry. For small α and ζ, one typically finds single-peaked or double-peaked profiles (Figure 18). For increased values of α and ζ, this switches to double peaks, with the peak separation increasing with increasing ζ. For large enough α and ζ, the second magnetic pole just becomes visible, and a third bump is obtained, in addition to two sharp peaks from the first magnetic pole. For example, a case of an intermediate value of α is shown in Figure 19, where less severe fading may allow photons from the opposite magnetic pole to become visible, thereby creating an additional small bump (Figure 19(f)). If ζ is close to 90°, one may obtain two double-peaked LCs, i.e., a four-peaked LC (Figure 20). In some cases, there is a sudden increase in the

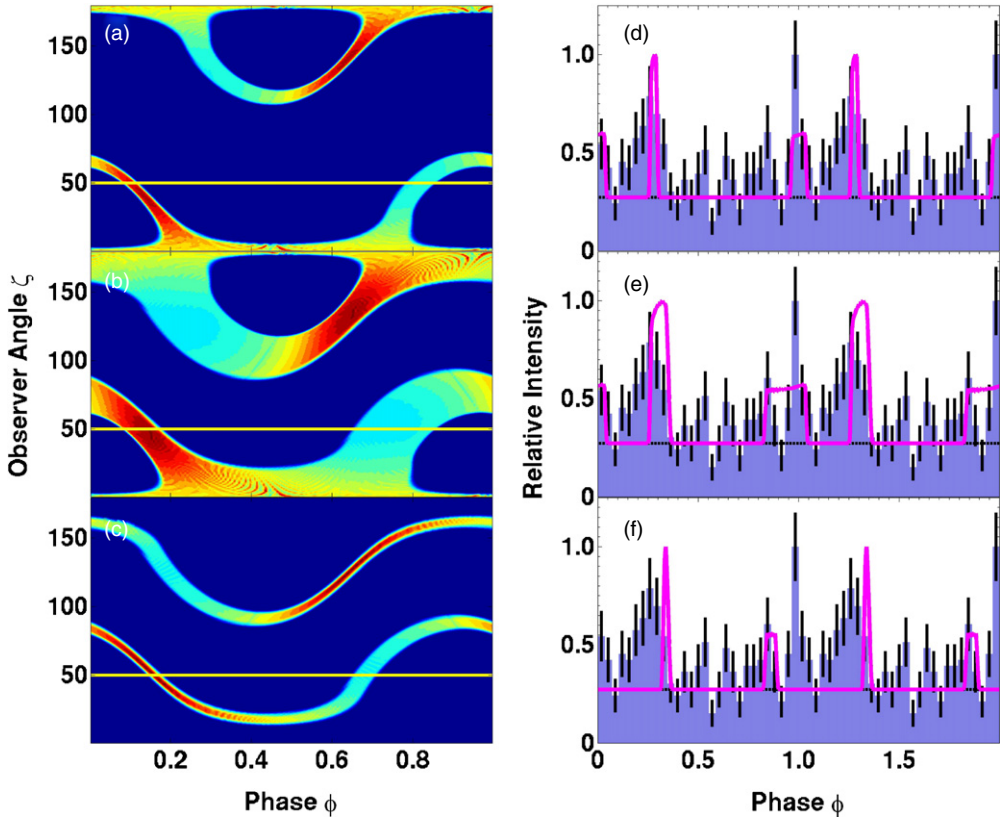

Figure 17. Constant-emissivity laSG model with low-altitude emission. The left column indicates phaseplots, while the right column indicates the corresponding model LCs, as well as the *Fermi* LAT profile (Ackermann et al. 2011) for PSR J0034−0534. Panels (a) and (d): $(R_{\rm min}, R_{\rm max}) = (0.12, 0.20)R_{\rm LC}$; panels (b) and (e): $(R_{\rm min}, R_{\rm max}) = (0.12, 0.40)R_{\rm LC}$; panels (c) and (f): $(R_{\rm min}, R_{\rm max}) = (0.30, 0.40)R_{\rm LC}$. We used $(\alpha, \zeta) = (30^\circ, 50^\circ)$, $(r_{\rm OVC,min}, r_{\rm OVC,max}) = (0.90, 0.95)$ implying $w = 0.05$, $\phi_0 = 0.18$, $P = 1.877$ ms, and gamma-ray background of nine events.

(A color version of this figure is available in the online journal.)

trailing peak due to the line of sight moving through the notch formed by the bunching of B-field lines in the retarded vacuum case (Dyks et al. 2004). Here, the magnetic field lines, and thus the radiation, are concentrated, leading to enhanced emission. One may therefore find values for α and ζ such that there will be four peaks of different sizes visible per rotation. This may potentially aid in modeling the complex radio profiles of some MSPs, although this will be limited by the phase separation and respective heights of the individual peaks. Lastly, when α is too large, the peak separation Δ is too small to fit the data for any choice of ζ, so that a large Δ constrains α to be smaller than some maximum.

It is usually less complicated to find best-fit laSG LC fits when searching manually ("by eye") than for the altitude-limited models, in the sense that there is less variation in profile shape. One only has to find the correct peak separation Δ (very sensitive to ζ) for reasonable-looking double-peaked profiles (determined by α and ζ). On the other hand, there are multiple combinations of the free parameters that give very similar LCs, so the solution is probably not unique. The different best-fit solutions usually are a trade-off between best fits for gamma-ray versus radio LCs. Indeed, we indicate two similar laSG solutions for the LCs of PSR J0034−0534, PSR J1939+2134, and PSR J1959+2048 in Figures 21, 22, and 23, respectively, and list some of the inferred parameters in Table 2. These are obtained by changing the fading parameters, but using very similar α and ζ.

Figure 21 shows fits for PSR J0034−0534 using laSG models. Here, "laSG1" means $(s_{\rm f}, \sigma_{\rm in}, \sigma_{\rm out}) = (1.2, 0.1, 0.3)R_{\rm NS}$, while "laSG2" is for $(s_{\rm f}, \sigma_{\rm in}, \sigma_{\rm out}) = (1.5, 0.2, 0.5)R_{\rm NS}$, for both gamma-ray and radio. (The choice of fading parameters $(s_{\rm f}, \sigma_{\rm in}, \sigma_{\rm out})$ for laSG1 and laSG2 will remain the same throughout, as well as the values of $r_{\rm OVC,min}$ and $r_{\rm OVC,max}$.) We used a gamma-ray background of nine events and a normalized radio background of 0.08. It is very important to note that we have shifted both gamma-ray and radio model profiles by a large normalized phase shift of $\phi_0 = 0.68$, which implies that the definitions of "leading peak" and "first peak" do not coincide anymore. By doing so, we could obtain a first peak (which is actually the trailing peak in the model, enhanced by caustic effects) that is higher than the second peak for this particularly small value of α. This provided a much better fit to the data. See Table 2 for a summary of best-fit parameters for all the LC fits.

In Figure 22, we show laSG model LC fits for PSR J1939+2134. We used $\phi_0 = 0.83$ for the radio and gamma-ray profiles, a gamma-ray background of 191.3 events, and a normalized radio background of 0.007. The widths of the laSG1 fit seem more optimal for reproducing the data and closely match the radio peak shapes. In order to obtain the correct relative heights for the radio peaks, one has to accept a smaller peak at phase ∼0.5 (in addition to using a large value for ϕ_0, similar to the case of PSR J0034−0534), which in turn does not reproduce the gamma-ray data all that well, although one has to bear in mind that the typical relative gamma-ray error is much larger than that of the radio. The laSG models are also not able to reproduce the off-peak gamma-ray LC features (e.g., at phase 0.2 and 0.7).

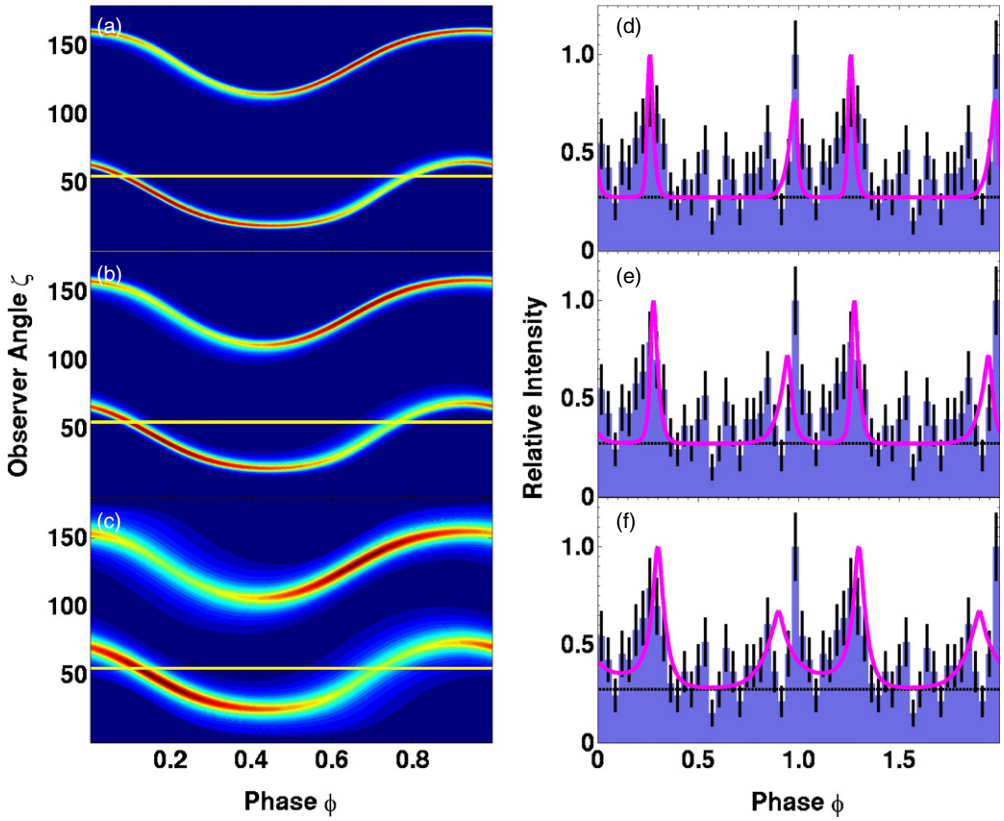

Figure 18. laSG model. The left column indicates phaseplots, while the right column indicates the corresponding model LCs as well as the *Fermi* LAT profile (Ackermann et al. 2011) for PSR J0034−0534. Panels (a) and (d): $(s_f, \sigma_{in}, \sigma_{out}) = (1.2, 0.1, 0.3)R_{NS}$; panels (b) and (e): $(s_f, \sigma_{in}, \sigma_{out}) = (1.5, 0.2, 0.5)R_{NS}$; panels (c) and (f): $(s_f, \sigma_{in}, \sigma_{out}) = (2.0, 0.8, 1.0)R_{NS}$. We used $(\alpha, \zeta) = (20^\circ, 55^\circ)$, $(r_{OVC,min}, r_{OVC,max}) = (0.90, 0.95)$ implying $w = 0.05$, $\phi_0 = 0.18$, $P = 1.877$ ms, and gamma-ray background of nine events. This figure illustrates that one usually have pulse shapes with broad first (leading) peaks, and sharp second (trailing) peaks in these cases, opposite to what is seen in the LC data of PSR J0034−0534.

(A color version of this figure is available in the online journal.)

The situation is opposite for laSG fits to the LCs of PSR J1959+2048 (Figure 23), where the model LCs now match the relative gamma-ray peaks better than those of the radio. Also, the broad first radio peak is difficult to reproduce, given the fading parameters used. We used $\phi_0 = 0.45$ and $\phi_0 = 0.46$ for the laSG1 and laSG2 models, a gamma-ray background of 53 events, and a normalized radio background of 0.005. As before, the emphasis has been to reproduce the two main peaks and not the off-peak emission.

It is important to emphasize that these laSG fits are not considered to be exhaustive, but are only for illustrational purposes. We wanted to show that the two main peaks may in principle come from a region nearby the stellar surface. It is conceivable that there may exist parameter combinations that would yield a better balance between optimal fits for the gamma-ray versus radio LCs, but this does not alter the main conclusion that the profiles may be reproduced by the laSG model for some combination of the free parameters.

6. DISCUSSION AND CONCLUSIONS

The aim of this paper was to study a third class of gamma-ray MSP LCs for which the gamma-ray and radio profiles are phase-aligned. This class is an addition to the two previously identified, where the radio profile either precedes or lags the gamma-ray one (Venter et al. 2009). While younger pulsars and the first two classes of MSPs may be modeled by gamma-ray emission regions extended over a large range of altitudes (OG/TPC/PSPC models) in conjunction with a conal radio beam at relatively lower emission altitudes, the LCs of the third class of MSPs indicate that the gamma-ray and radio emission should be co-located, and may exclusively originate either at high altitudes or at low altitudes relative to R_{LC}. We therefore studied the plausibility of reproducing the phase-aligned LCs using altitude-limited (high-altitude) versus laSG (low-altitude) geometric models. These classes of models provide a framework in which one may constrain the minimum and maximum emission altitudes of the radiation using the observed multi-wavelength LCs.

We introduced free parameters R_{min} and R_{max} in the alOG/alTPC models (both are free for radio emission region, but only R^{γ}_{max} is free for the gamma-ray emission region), and showed that the resulting profiles are sensitive to these variables. For example, it is possible to reduce off-peak emission and change peak widths by increasing R^{r}_{min} from the typical value of R_{NS} for TPC models and R_{NCS} for OG models, while relative peak heights may be fine-tuned (some peaks may even disappear) and low-level features may be emphasized by lowering R_{max}. We found fits from these models which could reproduce the salient features of the profiles, although not perfectly. We have demonstrated that we can limit the emission geometry, with typical errors on the emission altitudes being $\sim 0.3R_{LC}$, although R^{r}_{max} seems to be better constrained than R^{r}_{min}.

For the laSG models, we have demonstrated that a modulated emissivity at low altitudes can reproduce main features of the

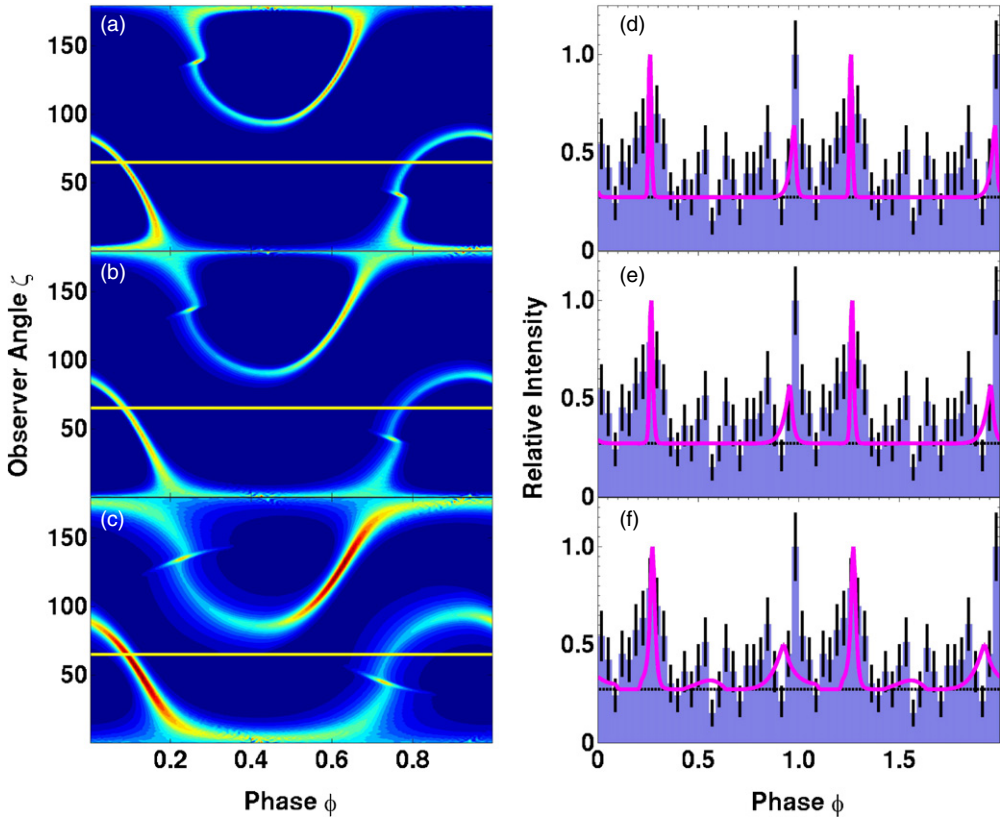

Figure 19. Same as Figure 18, but for $(\alpha, \zeta) = (40^\circ, 65^\circ)$.
(A color version of this figure is available in the online journal.)

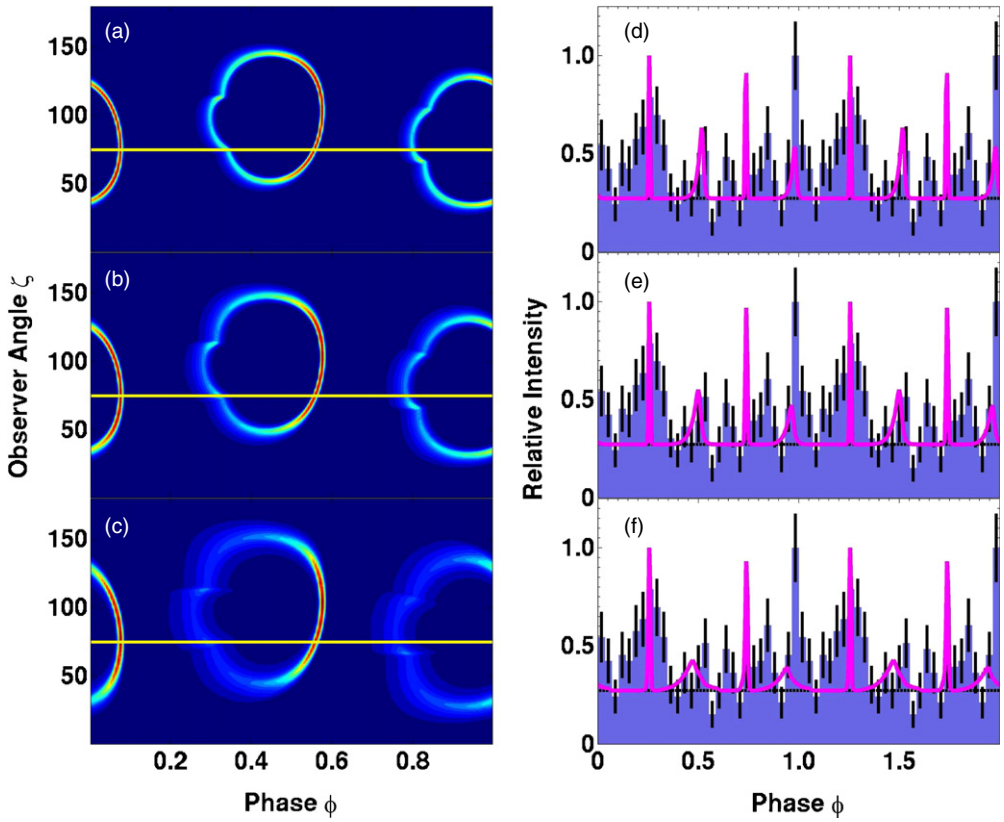

Figure 20. Same as Figure 18, but for $(\alpha, \zeta) = (80^\circ, 75^\circ)$. This illustrates the possibility of obtaining four peaks of different heights per rotation for certain choices of α and ζ.
(A color version of this figure is available in the online journal.)

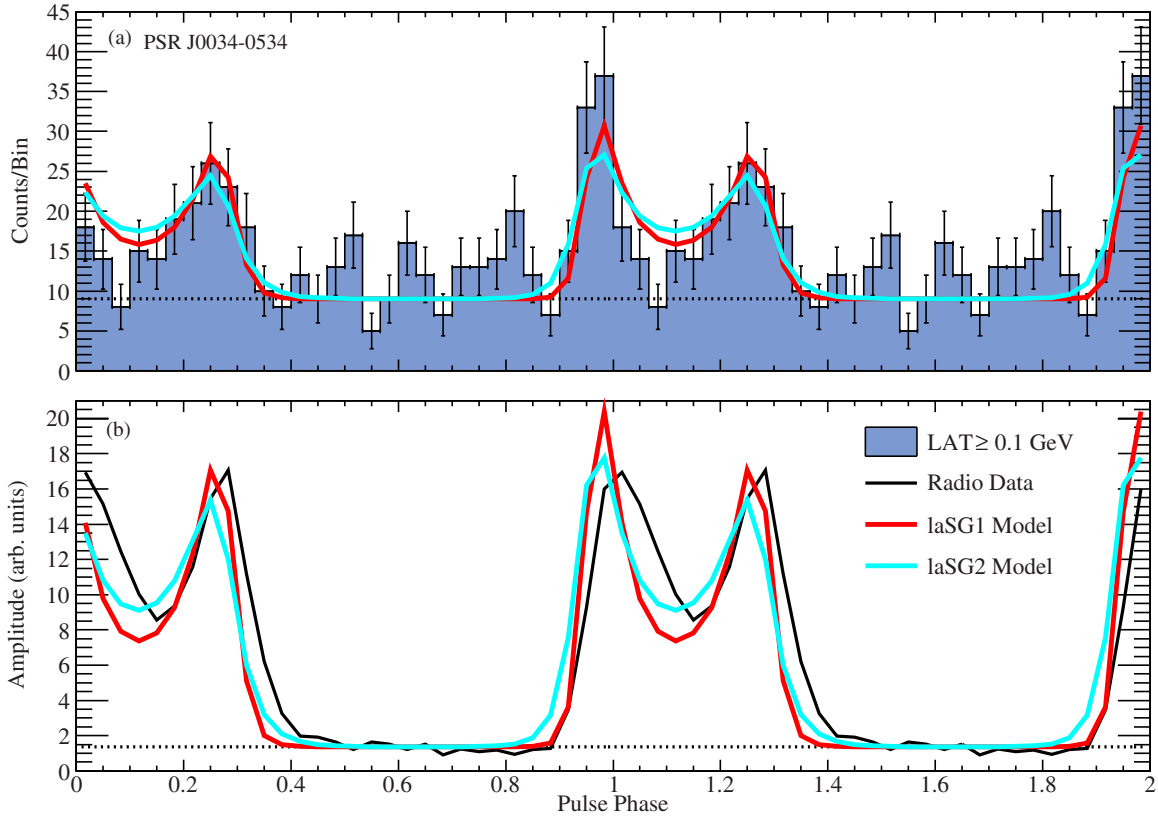

Figure 21. LC fits for PSR J0034−0534 using laSG models. Note that the large value of $\phi_0 = 0.68$ implies that the definition of "leading peak" and "first peak" do not coincide anymore. Our best-fit parameters are listed in Table 2 (where we also define "laSG1" and "laSG2"); also see the text for more details.
(A color version of this figure is available in the online journal.)

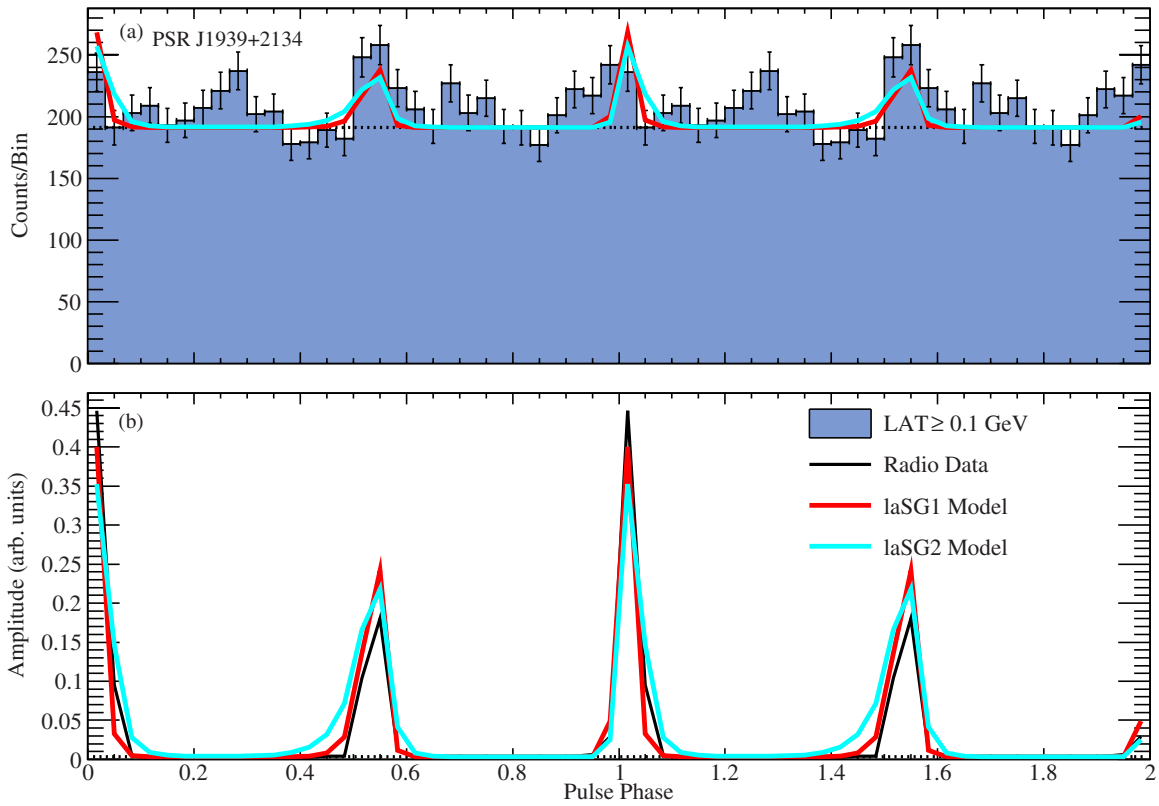

Figure 22. Same as Figure 21, but for PSR J1939+2134.
(A color version of this figure is available in the online journal.)

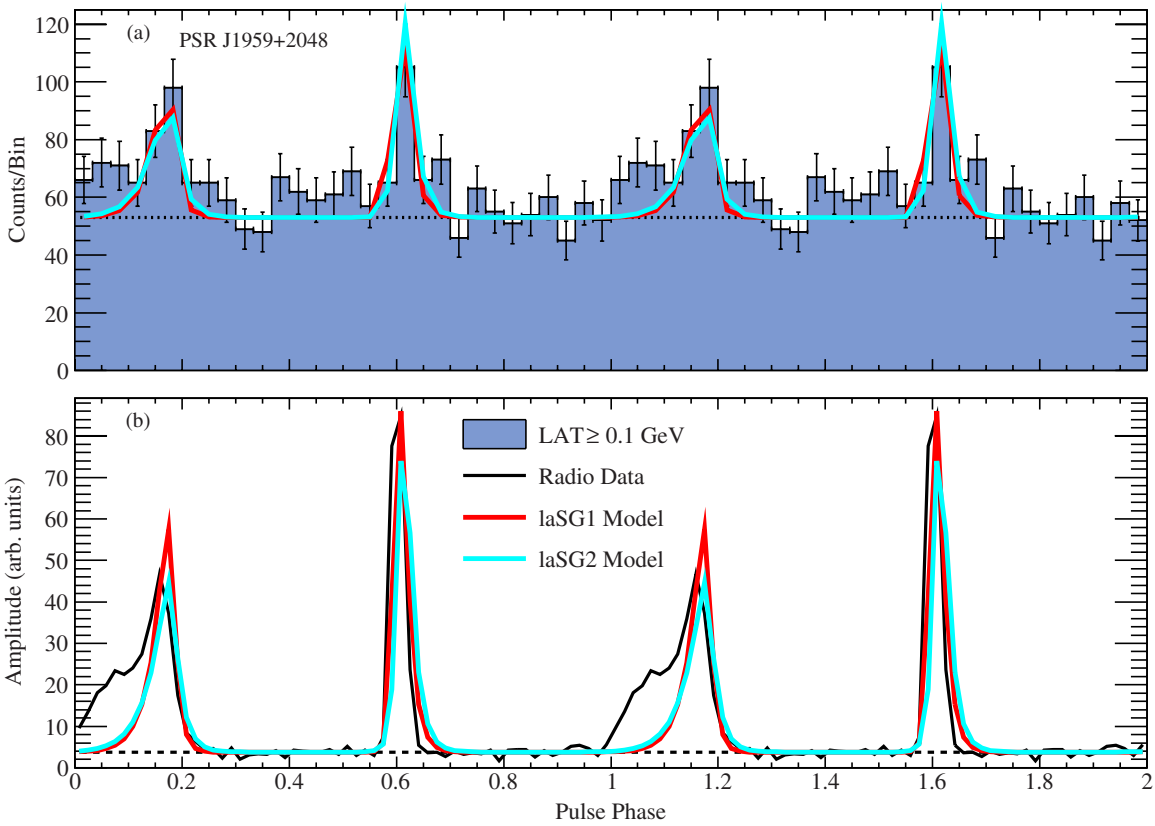

Figure 23. Same as Figure 21, but for PSR J1959+2048.
(A color version of this figure is available in the online journal.)

profiles quite well and that peak widths/phase positions may be tweaked using the fading parameters. Our conclusion that the trailing peak is enhanced by caustic effects and is therefore higher than the leading peak is independent of B-field structure to second order in $r/R_{\rm LC}$ or more because the emission occurs very close to the stellar surface. Thus, when modeling an LC such as that of PSR J0034−0534, one has to adjust the phase offset ϕ_0 so that the trailing peak becomes the first peak, in order to obtain the correct relative peak heights. This argues for a small α in this case.

One potentially limiting factor for the laSG models is that there is less variety of pulse shapes in this model compared to the altitude-limited outer-magnetosphere models. One may find good fits for the two sharp peaks typical of the pulsar LCs (reproducing the radio very closely in some cases), and even low-level bumps for some geometries, but not much diversity beyond these basic features. We found that there is typically a trade-off in better fitting the gamma-ray LC versus the radio one. Also, when finding a best fit for one set of fading parameters and a particular α and ζ, one may usually find another fit that is very close, but with different fading parameters and slightly different α and ζ. We therefore regard the inferred values of these free parameters as less robust than the case of the altitude-limited models. Therefore, we did not exhaustively search all combinations, as we deem it less useful to find a perfect fit with different sets of fading parameters for both the radio and gamma-ray LCs, given the large amount of free parameters. Development of a full radiation code with fewer free parameters should help to alleviate this problem.

In summary, we found reasonable fits to the LCs of PSR J0034−0534, PSR J1939+2134, and PSR J1959+2048 for both classes of models, as these can reproduce the main features of both the gamma-ray and radio LCs, as well as the phase alignment of these profiles. At the moment, it is difficult to quantitatively favor one class of models above the other, since searching for optimal laSG LC fits has not yet been implemented using the MCMC code as is the case for the altitude-limited models. However, we did calculate the likelihood of the best-fit laSG LCs. The alTPC models provide slightly better LC fits than the alOG models and both of these give better fits than the laSG models for the parameters listed (see Table 2). Favoring the alOG/alTPC models over the laSG model therefore implies that the phase-aligned gamma-ray and radio LCs are most probably of caustic origin, produced in the outer magnetosphere, and the radio emission is most likely originating near the light cylinder. Therefore, we can now divide the gamma-ray MSP population into three subclasses on the basis of their LCs: those with LCs fit by standard OG/TPC models, those with phase-aligned LCs fit by alOG/alTPC or laSG models, and those with LCs fit by PSPC models (these are referred to as LC Class I through III in Table 2).

If the altitude-limited models are taken to provide a good description of the LCs, the ideas regarding the presence of high-altitude (Manchester 2005), caustic radio emission (Ravi et al. 2010) will have been confirmed, implying that radio beams are very wide, similar to the gamma-ray beams. There are, however, some caveats to bear in mind. First, such caustic emission would result in nearly phase-aligned radio and gamma-ray profiles, and this idea will only be applicable to a subset of the pulsar population, including the Crab pulsar as well as some MSPs that exhibit LCs that are close in phase. Many of the *Fermi* pulsar population have quite large radio-to-gamma phase lags,

implying different emission regions for the radio and gamma rays in the pulsar magnetosphere. Since the gamma-ray profiles are believed to be of caustic origin, this rules out a caustic origin for radio emission of a large number of the gamma-ray pulsars, unless the radio emission region is significantly offset from the gamma-ray one in the pulsar magnetosphere, so that the height difference may introduce a phase offset (it is indeed possible to create modest phase lags—we estimate ∼0.1–0.2—by invoking different values for $R_{\rm min}$ and $R_{\rm max}$ for the radio and gamma-ray emission layers; see Figure 17). Radio emission occurring at relatively low altitudes in MSPs already exhibits caustic effects, depending on the particular height and extent of the emission region (see, e.g., Figure 11). It may therefore even be plausible to have caustic radio emission at lower altitudes and gamma rays coming from a region which extends up to $R_{\rm LC}$, with slightly phase-offset LCs (although it may not be possible to produce very large offsets in this scenario). Second, the shapes of the gamma-ray and radio LCs of most pulsars and MSPs are quite different. One typically observes double-peaked gamma-ray LCs and single-peaked radio ones. This complicates an explanation where the phase lag is attributed to radio caustic emission occurring at a lower altitude than that of the gamma rays: unless the radio emissivity has a strong altitudinal or azimuthal dependence, both radio and gamma-ray LCs would be mostly double-peaked, which is not observed. Attempting to fit the LCs of all known gamma-ray pulsars which are radio loud using altitude-limited models will further constrain the domain of applicability of this class of models, as will multi-wavelength pulse profile polarization properties (as described below).

Radio polarization measurements can be used to give independent constraints on the viewing geometry (Weltevrede et al. 2010), complementing the gamma-ray model fits. However, the RVM used to fit the radio position angle (P.A.) sweep across the profile assumes a static dipole magnetic field, with no rotation effects included (Radhakrishnan & Cooke 1969), and therefore would not be valid for the alTPC or alOG models where the radio peaks are caustics. In fact, even relatively low-altitude radio cone beam emission in MSPs will have significant distortions due to retardation and aberration so that the RVM is likely not valid in this case (Blaskiewicz et al. 1991). This may account for the generally poor or non-existent RVM fits of MSP polarization data.

Radio polarization measurements of PSR J0034−0534 (Stairs et al. 1999) find 0% linear polarization (and therefore no P.A. information) and very small circular polarization over the very broad pulse. Strong depolarization through the profile is predicted for the narrow double-peaked caustic LCs that occur for small α or ζ, where dips in polarization degree in the individual peaks merge together (Dyks et al. 2004). There are relatively good polarization measurements of PSR J1939+2134. Stairs et al. (1999) found rapid P.A. changes or mode switching and very low polarization degree in the first peak (interpulse), and high linear polarization and a rapid P.A. change at the leading edge of the second peak (main pulse). These polarization properties are generally confirmed by Yan et al. (2011), although they find more significant left-circular emission, particularly in the main pulse. Also, they find that the P.A. jump near the leading edge of the main pulse is closer to 60° rather than the 90° found previously, and for the first time detect an orthogonal transition near the trailing edge of the first peak. Such rapid P.A. swings coupled with depolarization is characteristic of caustic emission (Dyks et al. 2004), where the emission from a large range of altitudes and magnetic field orientation is compressed into a narrow phase interval to form the peaks. Finally, in the case of PSR J1959+2048, Thorsett & Stinebring (1990) measured 0% linear and ∼4% circular polarization, again rare and anomalous behavior for radio pulsars but potentially indicative of caustic effects. Polarization signatures therefore will be important to help discriminate between models with caustic emission (such as occurs in alOG/alTPC models) and non-caustic emission (e.g., in the laSG model).

Future studies should include development of full radiation models which will be able to reproduce both the multi-wavelength LC shapes, polarization properties, as well as the energy-dependent behavior of the spectra of the gamma-ray MSPs. In this vein, it might be necessary to invoke offset PCs of dipole magnetic fields, which have been shown to produce copious pair production in MSP magnetospheres (Harding & Muslimov 2011). High pair multiplicities at the PC are needed to set up the SG structure for both low-altitude pair cascades (laSG models) and high-altitude TPC-like emission. Higher multipole fields near the NS surface are possibly needed to create OGs in MSPs (Zhang & Cheng 2003). The presence of narrow gaps is motivated by the strikingly similar LCs of MSPs and young pulsars.

C.V. is supported by the South African National Research Foundation. A.K.H. acknowledges support from the NASA Astrophysics Theory Program. C.V., T.J.J., and A.K.H. acknowledge support from the *Fermi* Guest Investigator Program as well as fruitful discussions with Dick Manchester and Matthew Kerr. Portions of this work were performed by T.J.J. while he was a postdoc at the Naval Research Laboratory, sponsored by NASA DPR S-15633-Y. The *Fermi* LAT Collaboration acknowledges generous ongoing support from a number of agencies and institutes that have supported both the development and the operation of LAT as well as scientific data analysis. These include the National Aeronautics and Space Administration and the Department of Energy in the United States; the Commissariat à l'Energie Atomique and the Centre National de la Recherche Scientifique/Institut National de Physique Nucléaire et de Physique des Particules in France; the Agenzia Spaziale Italiana and the Istituto Nazionale di Fisica Nucleare in Italy; the Ministry of Education, Culture, Sports, Science, and Technology (MEXT), High Energy Accelerator Research Organization (KEK), and Japan Aerospace Exploration Agency (JAXA) in Japan; and the K. A. Wallenberg Foundation, the Swedish Research Council, and the Swedish National Space Board in Sweden. Additional support for science analysis during the operations phase is gratefully acknowledged from the Istituto Nazionale di Astrofisica in Italy and the Centre National d'Études Spatiales in France.

REFERENCES

Abdo, A. A., Ackermann, M., Ajello, M., et al. 2009, Science, 325, 848
Abdo, A. A., Ackermann, M., Ajello, M., et al. 2010a, ApJS, 187, 460
Abdo, A. A., Ackermann, M., Ajello, M., et al. 2010b, ApJ, 712, 957
Acharya, B. S., Bhat, P. N., Gandhi, V. N., Murthy, P. V. R., & Sathyanarayana, G. P. 1990, A&A, 232, L5
Ackermann, M., Ajello, M., Baldini, L., et al. 2011, ApJ, 726, 35
Alpar, M. A., Cheng, A. F., Ruderman, M. A., & Shaham, J. 1982, Nature, 300, 728
Arons, J. 1983, ApJ, 266, 215
Backer, D. C., Kulkarni, S. R., Heiles, C., Davis, M. M., & Goss, W. M. 1982, Nature, 300, 615
Backer, D. C., & Sallmen, S. T. 1997, AJ, 114, 1539
Bai, X.-N., & Spitkovsky, A. 2010, ApJ, 715, 1270
Bailes, M., Harrison, P. A., Lorimer, D. R., et al. 1994, ApJ, 425, L41

Bell, J. F., Kulkarni, S. R., Bailes, M., Leitch, E. M., & Lyne, A. G. 1995, ApJ, 452, L121
Blaskiewicz, M., Cordes, J. M., & Wasserman, I. 1991, ApJ, 370, 643
Brink, C., de Jager, O. C., Raubenheimer, B. C., et al. 1990, ApJ, 364, L37
Buccheri, R., Salamone, V., Bennett, K., et al. 1996, A&AS, 115, 305
Callanan, P. J., Van Paradijs, J., & Rengelink, R. 1995, ApJ, 439, 928
Chatterjee, S., Gaensler, B. M., Melatos, A., Brisken, W. F., & Stappers, B. W. 2007, ApJ, 670, 1301
Cheng, K. S., Ho, C., & Ruderman, M. 1986a, ApJ, 300, 500
Cheng, K. S., Ho, C., & Ruderman, M. 1986b, ApJ, 300, 522
Cognard, I., Guillemot, L., Johnson, T. J., et al. 2011, ApJ, 732, 47
Cusumano, G., Hermsen, W., Kramer, M., et al. 2003, A&A, 410, L9
Daugherty, J. K., & Harding, A. K. 1982, ApJ, 252, 337
Daugherty, J. K., & Harding, A. K. 1996, ApJ, 458, 278
Deutsch, A. J. 1955, Ann. d'Astrophys., 18, 1
Du, Y. J., Qiao, G. J., Han, J. L., Lee, K. J., & Xu, R. X. 2010, MNRAS, 406, 2671
Dyks, J., Harding, A. K., & Rudak, B. 2004, ApJ, 606, 1125
Dyks, J., & Rudak, B. 2003, ApJ, 598, 1201
Dyks, J., Wright, G. A. E., & Demorest, P. 2010, MNRAS, 405, 509
Eales, S. A., Becklin, E. E., Zuckerman, B., & McLean, I. S. 1990, MNRAS, 242, 17P
Fierro, J. M., Arzoumanian, Z., Bailes, M., et al. 1995, ApJ, 447, 807
Fraąckowiak, M., & Rudak, B. 2005, Adv. Space Res., 35, 1152
Fruchter, A. S., Gunn, J. E., Lauer, T. R., & Dressler, A. 1988a, Nature, 334, 686
Fruchter, A. S., Stinebring, D. R., & Taylor, J. H. 1988b, Nature, 333, 237
Gelman, A., & Rubin, D. 1992, Stat. Sci., 7, 457
Greaves, J. S., & Holland, W. S. 2000, MNRAS, 316, L21
Guan, Y., Fleissner, R., Joyce, P., & Krone, S. M. 2006, Stat. Comp., 16, 193
Guillemot, L., Cognard, I., Johnson, T. J., et al. 2011, in AIP Conf. Proc. 1357, Radio Pulsars: An Astrophysical Key to Unlock the Secrets of the Universe, ed. M. Burgay et al. (Melville, NY: AIP), 241
Guillemot, L., Johnson, T. J., Venter, C., et al. 2012, ApJ, 744, 33
Hall, T. A., Bond, I. H., Bradbury, S. M., et al. 2003, ApJ, 583, 853
Hansen, B. M. S., & Phinney, E. S. 1998, MNRAS, 294, 569
Harding, A. K., & Muslimov, A. G. 2011, ApJ, 726, L10
Harding, A. K., Usov, V. V., & Muslimov, A. G. 2005, ApJ, 622, 531
Hastings, W. K. 1970, Biometrika, 57, 97
Hewish, A., Bell, S. J., Pilkington, J. D. H., Scott, P. F., & Collins, R. A. 1968, Nature, 217, 709
Hirotani, K. 2006, ApJ, 652, 1475
Hirotani, K. 2007, ApJ, 662, 1173
Hobbs, G., Lorimer, D. R., Lyne, A. G., & Kramer, M. 2005, MNRAS, 360, 974
Huang, H. H., & Becker, W. 2007, A&A, 463, L5
Kinkhabwala, A., & Thorsett, S. E. 2000, ApJ, 535, 365
Kniffen, D. A., Hartman, R. C., Thompson, D. J., Bignami, G. F., & Fichtel, C. E. 1974, Nature, 251, 397
Knight, H. S., Bailes, M., Manchester, R. N., & Ord, S. M. 2005, ApJ, 625, 951
Kuiper, L., & Hermsen, W. 2003, arXiv:astro-ph/0312204
Kuiper, L., Hermsen, W., & Stappers, B. 2004, Adv. Space Res., 33, 507
Kuiper, L., Hermsen, W., Verbunt, F., et al. 2000, A&A, 359, 615
Kulkarni, S. R., & Hester, J. J. 1988, Nature, 335, 801
Kuzmin, A. D., & Losovsky, B. Ya. 2001, A&A, 368, 230
Lazio, T. J. W., & Fischer, J. 2004, AJ, 128, 842
Lundgren, S. C., Foster, R. S., & Camilo, F. 1996, in ASP Conf. Ser. 105, IAU Colloq. 160: Pulsars: Problems and Progress, ed. S. Johnston, M. A. Walker, & M. Bailes (San Francisco, CA: ASP), 497
Manchester, R. N. 2005, Ap&SS, 297, 101
Manchester, R. N., Hobbs, G. B., Teoh, A., & Hobbs, M. 2005, AJ, 129, 1993
Marinari, E., & Parisi, G. 1992, Europhys. Lett., 19, 451
Morini, M. 1983, MNRAS, 202, 495
Muslimov, A. G., & Harding, A. K. 2003, ApJ, 588, 430
Muslimov, A. G., & Harding, A. K. 2004a, ApJ, 606, 1143
Muslimov, A. G., & Harding, A. K. 2004b, ApJ, 617, 471
Muslimov, A. G., & Harding, A. K. 2009, ApJ, 692, 140
Muslimov, A. G., & Tsygan, A. I. 1992, MNRAS, 255, 61
Nicastro, L., Cusumano, G., Löhmer, O., et al. 2004, A&A, 413, 1065
Phinney, E. S., Evans, C. R., Blandford, R. D., & Kulkarni, S. R. 1988, Nature, 333, 832
Radhakrishnan, V., & Cooke, D. J. 1969, ApJ, 3, L225
Ransom, S. M., Ray, P. S., Camilo, F., et al. 2011, ApJ, 727, L16
Ravi, V., Manchester, R. N., & Hobbs, G. 2010, ApJ, 716, L85
Romani, R. W. 1996, ApJ, 470, 469
Romani, R. W. 2011, in AIP Conf. Proc. 1357, Radio Pulsars: An Astrophysical Key to Unlock the Secrets of the Universe, ed. M. Burgay et al. (Melville, NY: AIP), 205
Schönberner, D., Driebe, T., & Blöcker, T. 2000, A&A, 356, 929
Spitkovsky, A. 2006, ApJ, 648, L51
Stairs, I. H., Thorsett, S. E., & Camilo, F. 1999, ApJS, 123, 627
Stappers, B. W., Gaensler, B. M., Kaspi, V. M., Van der Klis, M., & Lewin, W. H. G. 2003, Science, 299, 1372
Thorsett, S. E., & Stinebring, D. R. 1990, ApJ, 361, 644
Van Paradijs, J., Allington-Smith, J., Callanan, P., et al. 1988, Nature, 334, 684
Venter, C., & De Jager, O. C. 2005, ApJ, 619, L167
Venter, C., Harding, A. K., & Guillemot, L. 2009, ApJ, 707, 800
Verbiest, J. P. W., Bailes, M., Coles, W. A., et al. 2009, MNRAS, 400, 951
Wang, Y., Takata, J., & Cheng, K. S. 2010, ApJ, 720, 178
Watters, K. P., Romani, R. W., Weltevrede, P., & Johnston, S. 2009, ApJ, 695, 1289
Weltevrede, P., Abdo, A. A., Ackermann, M., et al. 2010, ApJ, 708, 1426
Yan, W., Manchester, R. N., van Straten, W., et al. 2011, MNRAS, 414, 2087
Zavlin, V. E. 2006, ApJ, 638, 951
Zavlin, V. E. 2007, Ap&SS, 308, 297
Zhang, L., & Cheng, K. S. 2003, A&A, 398, 639
Zhang, L., Fang, J., & Chen, S. B. 2007, ApJ, 666, 1165
Zhu, C., Byrd, R. H., Lu, P., & Nocedal, J. 1997, ACM Trans. Math. Soft., 23, 550